System Frequency Dynamic Response of a Novel, Self-Synchronizing Inverter in a High Renewable Penetration Grid

by

Christian Perenyi

B.S. in Electrical Engineering

National Institute of Applied Sciences Lyon 2017

Submitted to the Graduate Faculty of the

Swanson School of Engineering in partial fulfillment

of the requirements for the degree of

Master of Science in Electrical and Computer Engineering

University of Pittsburgh

2020

UNIVERSITY OF PITTSBURGH

SWANSON SCHOOL OF ENGINEERING

This thesis was presented

by

Christian Perenyi

It was defended on

February 3, 2020

and approved by

Brandon M. Grainger, Ph.D., Assistant Professor,
Department of Electrical and Computer Engineering

Alexis Kwasinski, Ph.D., Associate Professor,
Department of Electrical and Computer Engineering

Ahmed Dallal, Ph.D., Assistant Professor,
Department of Electrical and Computer Engineering

Thesis Advisor: Brandon M. Grainger, Ph.D., Assistant Professor,
Department of Electrical and Computer Engineering

**System Frequency Dynamic Response of a Novel, Self-Synchronizing Inverter in a
High Renewable Penetration Grid**

Christian Perenyi, M.S.

University of Pittsburgh, 2020

In this thesis, a controller achieving current tracking objective without knowledge of the grid parameters is developed. An estimated rotating reference frame ($\gamma\delta$ -frame) is utilized. Within the control scheme, adaptive compensation terms facilitate the current tracking objective and, simultaneously, accounts for the unavailable grid voltage magnitude, grid frequency, and grid phase, hence eliminating the need for an additional measurement and feedback system for synchronization, such as a Phase-Locked Loop (PLL).

System frequency behavior using the controller in a high-renewable (low-inertia) grid indicates that the monitored performance metrics are significantly improved when compared to PLL-controlled, inverter-dominated grids.

Table of Contents

List of Tables

List of Figures

Acknowledgements

First, I would like to thank my entire family for supporting me all along my studies. They helped me to overcome all the challenges in my life. They have been there for supporting me during some difficult moments throughout my studies in France and abroad, they are part of my everyday life despite the geographical distance. Thanks also to my brother and sister, to my grand-parents my uncle for their encouragement and motivation they have been giving me during the past years.

This work wouldn't be possible without the collaboration of the University of Louisville with Mr. Joseph Latham, Mr. Moath Alqatamin, and especially Dr. Michael McIntyre.

I would like to thank Professor Dr. Brandon Grainger. You have been my mentor, my advisor, my academic guide. I am grateful for your guidance, your coaching, your understanding of my way of thinking. Hope to keep in touch and to be able to welcome you in France.

A special thank you to Thibaut Harzig for supporting me every day at work. You, with Sebastien, Camille and Büşra, are friends for a lifetime. Finally, thank you to the members of my committee Dr. Alexis Kwasinski and Dr. Ahmed Dallal and my lab mates: Alvaro Cardoza, Zachary Smith, Santino Graziani Tom Cook, Erick Bittenbender, John Kieffer, Adam Emes, Ryan Brody, Jenna Delozier, Corey Weinmann and Rui Hu.

Thanks also to Monica Miranda Cuenca coming from France to attend my defense.

1.0 Introduction

In today's economy, energy transition is one of Europe's top priorities. A main component of this challenge is to install a cleaner portfolio of renewable energy resources such as photovoltaic (PV) systems and wind turbines. That is why, the penetration ratio, Pr, of the renewable energy over the total energy generation (fossil + renewable) is significantly increasing; based on the German Energiewende, Germany will have a Pr of 80% by 2050 compared to 31.6% in 2016 [1].

To optimally integrate these renewable resources, it is necessary to rethink the electric power grid itself by adjusting the centralized generation model and progressively transitioning to a distributed generation (DG) based power grid architecture through power electronics and their control. Droop control, [2] a widely adopted method to integrate variable renewable sources (VRSs), is a decentralized and communication-less control, contributing to the overall frequency (and voltage) control by emulating virtual inertia (and a virtual impedance) [3]. However, the expansion of renewable energy inevitably drops the mechanical inertia of the whole power system because these generation resources cannot store kinetic energy as they do not have a rotating mass [4]. Hence, a mismatch between generation and consumption cannot always be mechanically compensated for which can cause large frequency swings. For system operation, loads and renewable sources should not be tripped [5].

To perform a DG interconnection, the inverter will convert the DC voltage and current to AC that matches the exact phase, frequency and magnitude of the grid voltage. If not, the inverter-based source may trip. The phase and frequency need to be determined by a phase-lock loop (PLL). Synchronous reference frame PLLs are widely applied in three-phase distributed generation systems. This synchronization method is the most widely proposed solution because the technique

1

provides excellent results for balanced grid conditions but becomes quite sensitive to unbalances and harmonic disturbances in grid voltage [6], [7]. One reason for this drawback is that modern power converters require fast detection and accurate knowledge of the grid angle [6]. For faster angle detection, increasing the bandwidth of a PLL has been considered, [8], but is limited by the presence of other converters operating nearby [9], weaker grid conditions tied to short circuit ratios [9], [7], and large penetration levels of DG units which can correspond to low-frequency power oscillations and system instabilities [7]. Many of the attempts to design a better PLL to handle such conditions have not considered the coupling effects and interactions between the PLL and system impedance network, which impacts PLL tuning [8]. This coupling has the potential to lead to instability issues when multiple inverters are connected together [7]. Other grid stability issues resulting from PLL schemes under various grid conditions, like islanding, are reported in [7].

Additional hardware like voltage sensors required for PLL-type systems are expensive and introduce electrical noise and dc offsets which require compensation. A PLL system is a self-contained feedback loop that is outside the primary current control scheme, hence creating a cascaded control architecture [10]. For optimal stability and accuracy, the current control scheme should be knowledgeable of the error dynamics of the PLL system.

Most commercial PV inverters operate as grid-following (GFL) sources that regulate their output power by measuring the angle of the grid voltage using a PLL. These units simply follow the grid frequency and do not actively control their frequency output. In contrast, a grid-forming source (GFM) controls its frequency and voltage output. However, as GFM sources retire and are replaced with renewable based generation, GFLs begin to dominate the electric grids leading to the common problems initiated by the PLL unit. For one cause for concern with increased GFLs, consider the state of California in the United States. In one reported event, California had

2

experienced significant loss of generation, ~700MW, because the inverter PLL detected frequencies less than 57 Hz and initiated an instantaneous trip. However, the lowest measured frequency only dropped to 59.87 Hz. As [11] points out, engineers need to develop solutions for the reliable operation of inverter-dominated power systems. GFM will play a constructive role in improving frequency dynamics and stability of inverter-dominated power systems. A key conclusion from [11] is that GFL inverters result in reduced damping and higher frequency excursions with increases in inverter penetration. GFM inverters, on the contrary, will result in increased damping and lower peak frequency excursions with increases in inverter penetration.

Given these considerations, a grid synchronizing control technique that requires an inverter to behave like a grid forming source with no PLL is an essential requirement in grid power electronic systems. In this article, a unique approach is provided for self-synchronizing, GFL inverters requiring no PLL, one three-phase current measurement, and can be modified to behave as a GFM inverter. The contribution of this work is to present results, in a highly-renewable and low-inertia grid, indicating that the discussed self-synchronizing control scheme can improve DG grid stability compared to traditional PQ reference PLL (PQ-PLL) controlled inverters.

2.0 Grid Model

2.1 Two-Sourced Reduced Model

In order to model the entire power-grid, a two-source, reduced-order (Figure 1) modelling approach is used in this work. The inverter voltage source (Figure 1) aims to represent the inverter-based renewable sources where the source itself is modeled as a constant DC source. This strong assumption, which implies that the dynamics linked to the source are ignored, can be justified since emphasis is put on inverter dynamics. The inverter model and dynamics will be studied in the next part.
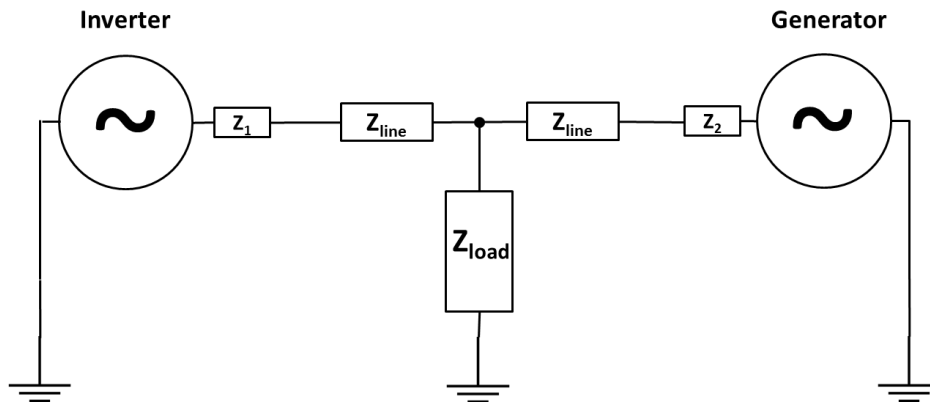
Figure 1 - Two-Sourced Reduced Model

2.2 Generator Model

The machine is a synchronous steam generator often used to represent fossil-based generators. The machine model accounts for the turbine, a governor and an exciter. An IEEE Type

4

1 DC1A model, without the saturation function, is used to model the synchronous machine and the automatic voltage regulator (AVR). Based on [12], the governor, the non-reheat steam turbine, and the machine inertia are modeled as first order systems. Both per unit machine blocks (Figure 2) are first order approximations (e.g. stator transients are neglected) of the full steam turbine model.
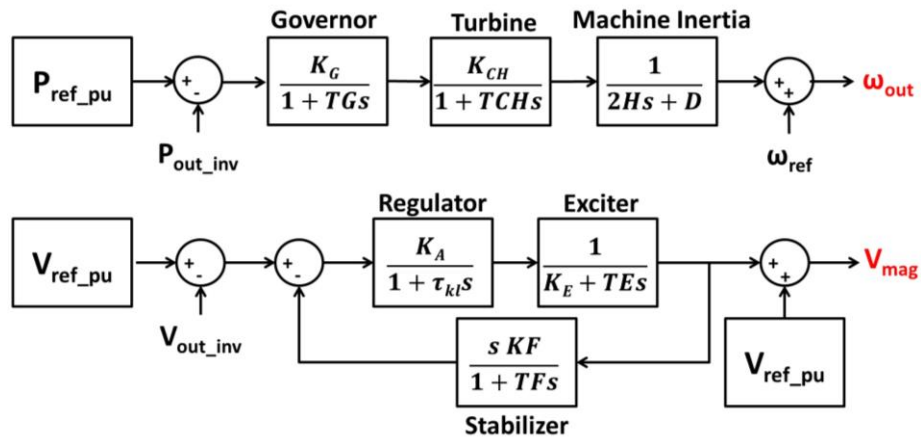
Figure 2 - Generator Dynamics

2.2.1 Governor-Turbine Detailed Model
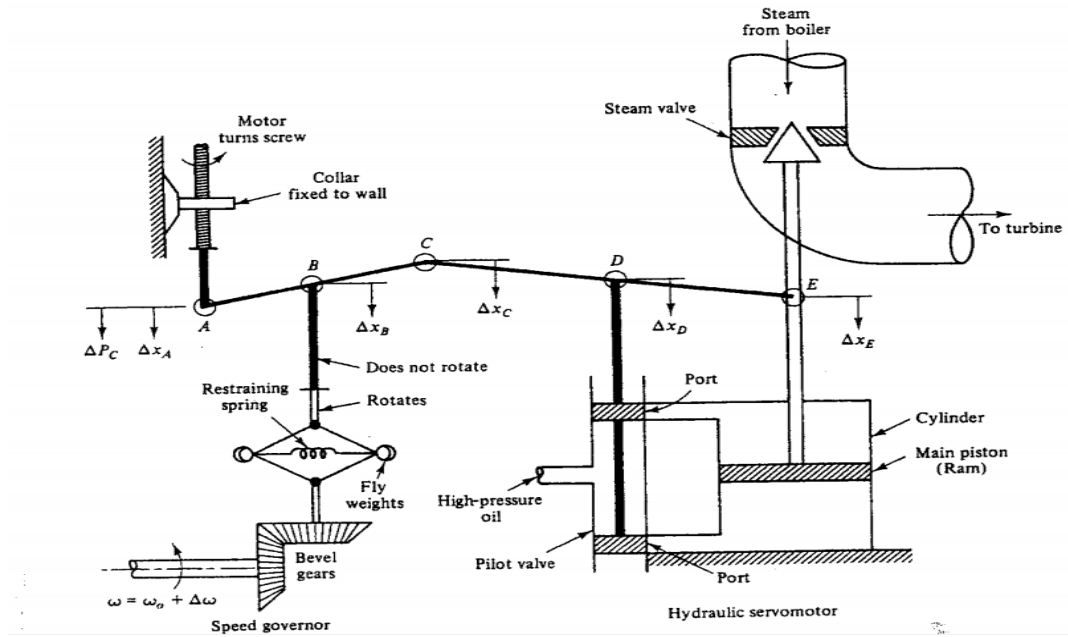
Figure 3 - Servo-Assisted Speed Governor [12]

A servo-assisted speed governor is presented in Figure 3. We define Δx_A, Δx_B, Δx_C, Δx_D, Δx_E as small change in position from nodes A, B, C, D and E respectively. For a linearized model of the speed-governor around the operating point, node A, B and C are on the same line so that C depends from Δx_A, Δx_B:

$$\Delta x_C = k_B \Delta x_B - k_A \Delta x_A = k_1 \Delta \omega - k_2 P_c \tag{2.1}$$

where k_1, k_2 are constants depending on length of different arms of the mechanism. In the same way, in the linearized system, nodes C, D and E are int the same line so:

$$\Delta x_D = k_3 \Delta x_C - k_4 \Delta x_E \tag{2.2}$$

6

where k_3, k_4 are constants depending on length of different arms of the mechanism. Concerning the servomotors dynamics, we assume that the high-pressure oil flow rates is proportional to Δx_D, so:

$$\frac{d\Delta x_E}{dt} = -k_5 \Delta x_D \tag{2.3}$$

where k_5 is based on the oil pressure and the geometry of the servomotor. Taking the Laplace transform of (2.3) and replacing (2.1) and (2.2) into (2.3) we can derive:

$$\Delta \hat{x}_E = \frac{k_2 k_3 k_5}{s + k_4 k_5}\left(\Delta \hat{P}_c - \frac{k_1}{k_2}\Delta \hat{\omega}\right) = \frac{K_G}{1 + T_G s}\left(\Delta \hat{P}_c - \frac{1}{R}\Delta \hat{\omega}\right) \tag{2.4}$$

where $K_G = \frac{k_2 k_3}{k_4}$, $T_G = \frac{1}{k_4 k_5}$ and $R = \frac{k_2}{k_1}$. For our model, $\frac{1}{R}\Delta \hat{\omega} = P_{out\_inv}$ because of the droop control which is on the inverter side.

A simplified approach will be presented for the steam turbine modelling. Let's imagine a small positive step increase in x_E. In steady state, ΔP_m (output of the steam turbine) will also be a positive constant but there is a delay since the increased flow does not penetrate instantaneously into all the blades of the turbine. This approach is highly simplified because the real behavior is complex and is not a focus of this work. This way, we can approximate the non-reheat turbine by a first order transfer function. The time constant and the gain can be taken in data-sheets or be set based on experimental data.
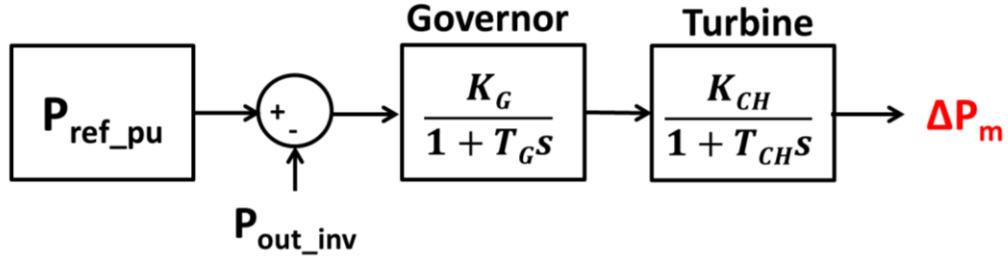
Figure 4 - Governor-Turbine Block Diagram

2.2.2 Generator Inertia Modelling

The change of the grid load directly impacts the electrical power output which is proportional to the output torque T_e of the generator causing a mismatch between the output torque T_e and the mechanical torque T_m. This phenomenon is described by the swing equation:

$$J\frac{d\Delta\omega_r}{dt} = T_m - T_e \tag{2.5}$$

where J is the total moment of inertia of the rotor mass and ω_r the rotor speed. Knowing that:

$$P_m - P_e = \omega_r(T_m - T_e) \tag{2.6}$$

and replacing (2.6) into (2.5), we get:

$$P_m - P_e = M\frac{d\Delta\omega_r}{dt} \tag{2.7}$$

where $M = J\omega_r$ and is the inertia constant of the machine. In order to normalize this equation, we introduce:

$$H = \frac{J\omega_s^2}{2S_{rated}}$$

(2.8)

where S_{rated} is the three phase rating of the machine and ω_s the synchronous speed. Since in steady state $\omega_r = \omega_s$, we can write:

$$\frac{2H}{\omega_s}\frac{d^2\delta}{dt^2} = P_m - P_e$$

(2.9)

where:

$$\delta = \theta_r - \omega_s t$$

(2.10)

where:

$$\frac{d\theta_r}{dt} = \omega_r$$

(2.11)

The electrical grid is composed of both frequency-dependent loads like motors and non-frequency dependent loads like for example restrictive loads. That is why, the overall delta of the electrical power depends on both types of loads such as:

$$\Delta P_e = \Delta P_l + \Delta P_L = \Delta P_l + D\Delta\omega_r$$

(2.12)

where $D = \frac{\Delta P_L}{\Delta \omega_r}$ is the load damping constant expressed in percentage, ΔP_l is the non-depend

frequency load change and ΔP_L is the depend frequency load change. The damping effect needs to

be taken in account.

The overall generator frequency dynamics are presented in Figure 5.
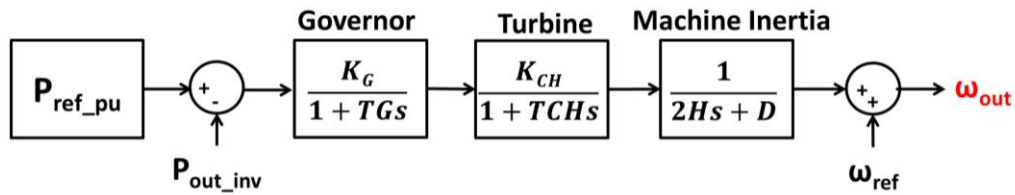
Figure 5 - Overall Generator Frequency Dynamics

2.2.3 Excitation System Model
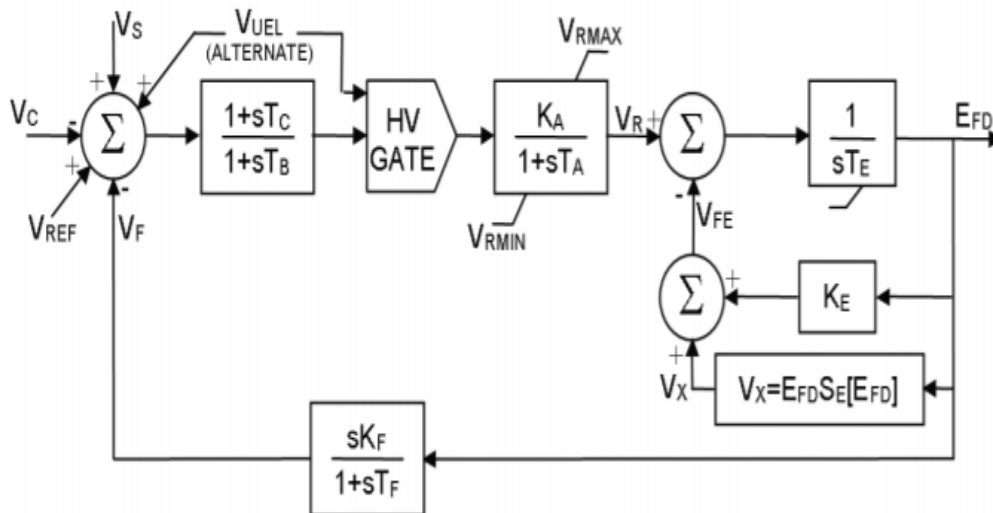
Figure 6 - IEEE Type 1 DC1A Model [13]

The excitation model is extracted from IEEE standards [13]. In this standard ("IEEE Recommended Practice for Excitation System Models for Power System Stability Studies") different detailed exciter systems models are presented: direct current commutator exciters, alternator-supplied rectifier excitation systems and static excitation systems. A direct current commutator exciter has been selected for this work because its wide use and its simplicity; specifically we will be using the - IEEE Type 1 DC1A model. For our study, we decided to remove the saturation model to avoid complexity since the saturation had not a considerable effect on the system for this application.

2.3 Load Model

The three phase load is composed of an inductor and resistor in series (Figure 7). Line impedance is negligible compared to the load impedance.
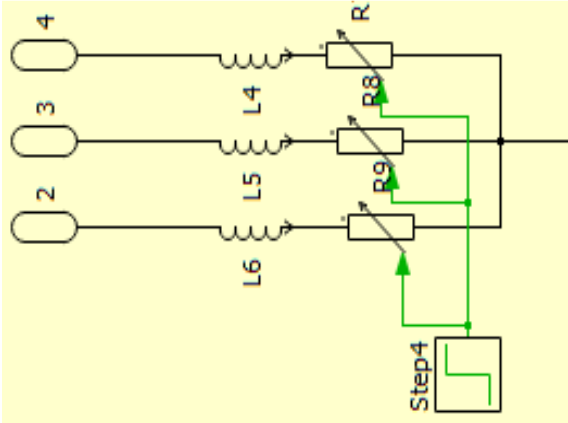
Figure 7 – Load Model

11

3.0 Inverter System Model

3.1 General Model Background

3.1.1 Inverter Model and Average Model
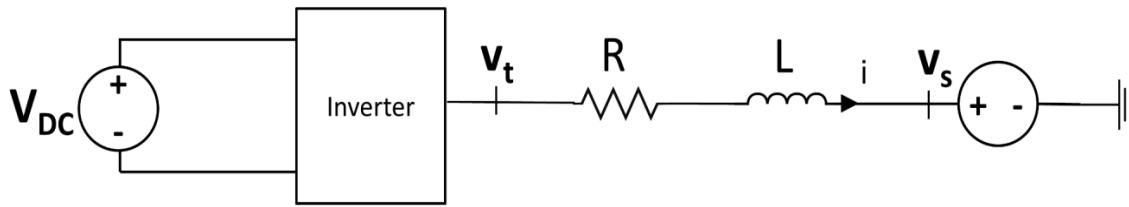
Figure 8 – One Phase Inverter Circuit

Let's start studying a single phase converter model (Figure 8). The dynamic equation of the output current is represented by (3.1).

$$L\frac{di(t)}{dt} + \text{Ri}(t) = V_t(t) - V_s(t) \tag{3.1}$$

where $Vs\,(t) = Vs\cos(\omega t)$ corresponds to the voltage of the grid in Figure 8. This voltage is considered as constant during a switching interval T_s.

Based on the superposition principle (3.4), the output current can be considered as the summation of a DC component (3.2) - steady state component, and an AC component (3.3) used for small signal analysis.

$$L\frac{d\overline{\iota(t)}}{dt} + \text{R}\overline{\iota(t)} = \frac{V_{DC}}{2}(2\text{d}(t) - 1) - V_s(t) \tag{3.2}$$

12

$$L\frac{d\widetilde{\imath(t)}}{dt} + R\widetilde{\imath(t)} = \sum_{h=1}^{h=+\infty} a_h \cos(h\omega_s t) + b_h \sin(h\omega_s t) \tag{3.3}$$

$$i(t) = \overline{\imath(t)} + \widetilde{\imath(t)} \tag{3.4}$$

d(t) being the duty cycle at time during the switching period T_s. However, for our study we can neglect the impact of $\widetilde{\imath(t)}$ over i(t).

In order to extend this method for cases where average variables are themselves function of time, the averaging operator is defined as:

$$\overline{x(t)} = \frac{1}{T_s}\int_{t-T_s}^{t} x(\tau)d\tau, \tag{3.5}$$

where $\overline{x(t)}$ is the average value of $x(t)$ over the period T_s. This operator can be applied on both side of (3.2) if the frequency of the carrier signal ω_s is at least 10 times higher than the modulating signal which gives:

$$L\frac{d\overline{\imath(t)}}{dt} + R\overline{\imath(t)} = m(t)\frac{V_{DC}}{2} - V_s(t) \tag{3.6}$$

where m(t)=Mcos(ωt) and M=(2$\bar{d}$ − 1), that way the modulation index describes the relationship between the magnitude of the modulating signal and the duty ratio. For this study, the module of m should not exceed 1 to avoid saturation. Other strategies such as space vector modulation, where m can eventually go beyond 1. In this case the maximum voltage output value is $\frac{V_{DC}}{2}$.

Similarly, for a three phase inverter dynamic equations remain the same for phase a and have a $\pm \frac{2\pi}{3}$ phase shift for phase b and c.

$$
\begin{cases}
L\dfrac{d\overline{\iota_a(t)}}{dt} + R\overline{\iota_a(t)} = M_a\dfrac{V_{DC}}{2}\cos(\omega t) - V_s\cos(\omega t) & (3.7) \\[2ex]
L\dfrac{d\overline{\iota_b(t)}}{dt} + R\overline{\iota_b(t)} = M_b\dfrac{V_{DC}}{2}\cos\left(\omega t - \dfrac{2\pi}{3}\right) - V_s\cos\left(\omega t - \dfrac{2\pi}{3}\right) & (3.8) \\[2ex]
L\dfrac{d\overline{\iota_c(t)}}{dt} + R\overline{\iota_c(t)} = M_c\dfrac{V_{DC}}{2}\cos\left(\omega t + \dfrac{2\pi}{3}\right) - V_s\cos\left(\omega t + \dfrac{2\pi}{3}\right) & (3.9)
\end{cases}
$$

To achieve the desired output value a control needs to be implemented since all parameters can change in time especially the grid voltage V_s or in another configuration the load and so the required output current. That way, a sinusoidal command tracking needs to be designed which implicate really elaborate compensators and a really wide bandwidth. We also need a fast dynamic behavior and a small steady-state error.

DC tracking problems have widely been studied due to their simplicity. All the requirements mentioned above can be completed with a simple PI compensator. That is why, we are willing to transform our rotating values to DC values. The Park's transform can do that; moving from a rotating abc-frame to a DC dq-frame.

3.1.2 dq-Transform

This part is purely theoretical. It can be applied to any time varying function of a balanced system. It is important to understand how the dq-frame is built and what does it geometrically represents.

So, let's consider a time varying function f(t) in a three phase balanced system with a constant amplitude f.

$$\begin{cases} f_a(t) = f\cos(\omega t + \theta_0) & (3.10) \\ f_b(t) = f\cos\left(\omega t - \dfrac{2\pi}{3} + \theta_0\right) & (3.11) \\ f_b(t) = f\cos\left(\omega t + \dfrac{2\pi}{3} + \theta_0\right) & (3.12) \end{cases}$$

The space vector representation of this system is:

$$\overrightarrow{f(t)} = \frac{2}{3}\left(f_a(t) + f_b(t)e^{j\frac{2\pi}{3}} + f_c(t)e^{j\frac{4\pi}{3}}\right) = (fe^{j\theta_0})e^{j\omega t} = \underline{f}e^{j\omega t} \qquad (3.13)$$

This space vector $\overrightarrow{f(t)}$ is represented by a magnitude and an angle. Another representation would be to characterize its real and imaginary part:

$$\overrightarrow{f(t)} = f_\alpha(t) + jf_\beta(t) \qquad (3.14)$$

Clark's transform gives us the transfer matrix from abc-domain to αβ-domain is:

$$\begin{bmatrix} f_\alpha(t) \\ f_\beta(t) \end{bmatrix} = \frac{2}{3}C \begin{bmatrix} f_a(t) \\ f_b(t) \\ f_c(t) \end{bmatrix} = \frac{2}{3}\begin{bmatrix} 1 & -\dfrac{1}{2} & -\dfrac{1}{2} \\ 0 & \dfrac{\sqrt{3}}{2} & -\dfrac{\sqrt{3}}{2} \end{bmatrix}\begin{bmatrix} f_a(t) \\ f_b(t) \\ f_c(t) \end{bmatrix} \qquad (3.15)$$

Identically, you can go from $\alpha\beta$-frame to the abc-frame by applying Clark's transpose matrix:

$$\begin{bmatrix} f_a(t) \\ f_b(t) \\ f_c(t) \end{bmatrix} = \begin{bmatrix} 1 & 0 \\ -\dfrac{1}{2} & \dfrac{\sqrt{3}}{2} \\ -\dfrac{1}{2} & -\dfrac{\sqrt{3}}{2} \end{bmatrix}\begin{bmatrix} f_\alpha(t) \\ f_\beta(t) \end{bmatrix} \qquad (3.16)$$

So now we have a new $\alpha\beta$-frame with only two components. However, this frame is still rotating. We are going to introduce a rotating dq-frame from which the rotating values will look constant. It is defined the following way:

$$f_d(t) + jf_q(t) = (f_\alpha(t) + jf_\beta(t))e^{-j\epsilon(t)} \tag{3.17}$$

We introduce a time-dependent phase shift $-\epsilon(t)$ on the space-vector $\overrightarrow{f(t)}$. Based on Euler's identities:

$$\begin{bmatrix} f_d(t) \\ f_q(t) \end{bmatrix} = \begin{bmatrix} \cos \epsilon(t) & \sin \epsilon(t) \\ -\sin \epsilon(t) & \cos \epsilon(t) \end{bmatrix} \begin{bmatrix} f_\alpha(t) \\ f_\beta(t) \end{bmatrix} \tag{3.18}$$

Now to go directly from the abc-frame to the dq-frame we use the Park's transformation:

$$\begin{bmatrix} f_d(t) \\ f_q(t) \end{bmatrix} = \frac{2}{3} \begin{bmatrix} \cos \epsilon(t) & \sin \epsilon(t) \\ -\sin \epsilon(t) & \cos \epsilon(t) \end{bmatrix} \begin{bmatrix} 1 & -\frac{1}{2} & -\frac{1}{2} \\ 0 & \frac{\sqrt{3}}{2} & -\frac{\sqrt{3}}{2} \end{bmatrix} \begin{bmatrix} f_a(t) \\ f_b(t) \\ f_c(t) \end{bmatrix} \tag{3.19}$$

$$\begin{bmatrix} f_d(t) \\ f_q(t) \end{bmatrix} = \frac{2}{3} \begin{bmatrix} \cos \epsilon(t) & \cos\left(\epsilon(t) - \frac{2\pi}{3}\right) & \cos\left(\epsilon(t) - \frac{4\pi}{3}\right) \\ \sin \epsilon(t) & \sin\left(\epsilon(t) - \frac{2\pi}{3}\right) & \sin\left(\epsilon(t) - \frac{4\pi}{3}\right) \end{bmatrix} \begin{bmatrix} f_a(t) \\ f_b(t) \\ f_c(t) \end{bmatrix} \tag{3.20}$$

It is essential to choose the correct value of $\epsilon(t)$ so the phasor and the frame rotate at the same speed.

3.1.3 Dynamic Model of the VSC – dq-Frame

It is useful to represent the three phase dynamic equation with phasors under the assumption that the system is balanced.

$$L\frac{\overrightarrow{di(t)}}{dt} + \overrightarrow{Ri(t)} = \frac{V_{DC}}{2}\overrightarrow{m(t)} - \overrightarrow{V_s} \qquad (3.21)$$

Applying Park's transformation (3.19), we can these equations into a rotating frame:

$$\begin{cases} L\dfrac{di_d}{dt} - L\dfrac{d\varepsilon(t)}{dt}I_q + Ri_d = m_d\dfrac{V_{DC}}{2} - V_{sd} & (3.22) \\ L\dfrac{di_q}{dt} + L\dfrac{d\varepsilon(t)}{dt}I_d + Ri_q = m_q\dfrac{V_{DC}}{2} - V_{sq} & (3.23) \end{cases}$$

By setting $\varepsilon(t) = \omega t + \theta_0$, we can simplify the equations (3.22) and (3.23)

$$\begin{cases} L\dfrac{di_d}{dt} - L\omega I_q + Ri_d = m_d\dfrac{V_{DC}}{2} - V_{sd} & (3.24) \\ L\dfrac{di_q}{dt} + L\omega I_d + Ri_q = m_q\dfrac{V_{DC}}{2} - V_{sq} & (3.25) \end{cases}$$

As seen in the previous part, the objective of using Park's transform is that the signal values (current, voltage, modulation index) are constant values in a synchronous rotating frame. That is why, at steady state we have:

$$\begin{cases} L\omega I_q + Ri_d = m_d\dfrac{V_{DC}}{2} - V_{sd} & (3.26) \\ L\omega I_d + Ri_q = m_q\dfrac{V_{DC}}{2} - V_{sq} & (3.27) \end{cases}$$

3.2 Benchmark #1 – PQ Inverter Control with a PLL (PQ-PLL)

PQ-PLL control (Figure 9) is a widely used control routine, which tracks real and reactive power references. The power references are then altered and used as current references in the *dq*-frame. Here, the PLL output phase angle serves a critical role in obtaining these time-independent references. The detailed control is developed in [14] and per unitized for the present application. Both *d* and *q*-axis compensators set the system dynamics while the feed forward filters prevent a peak current at startup.
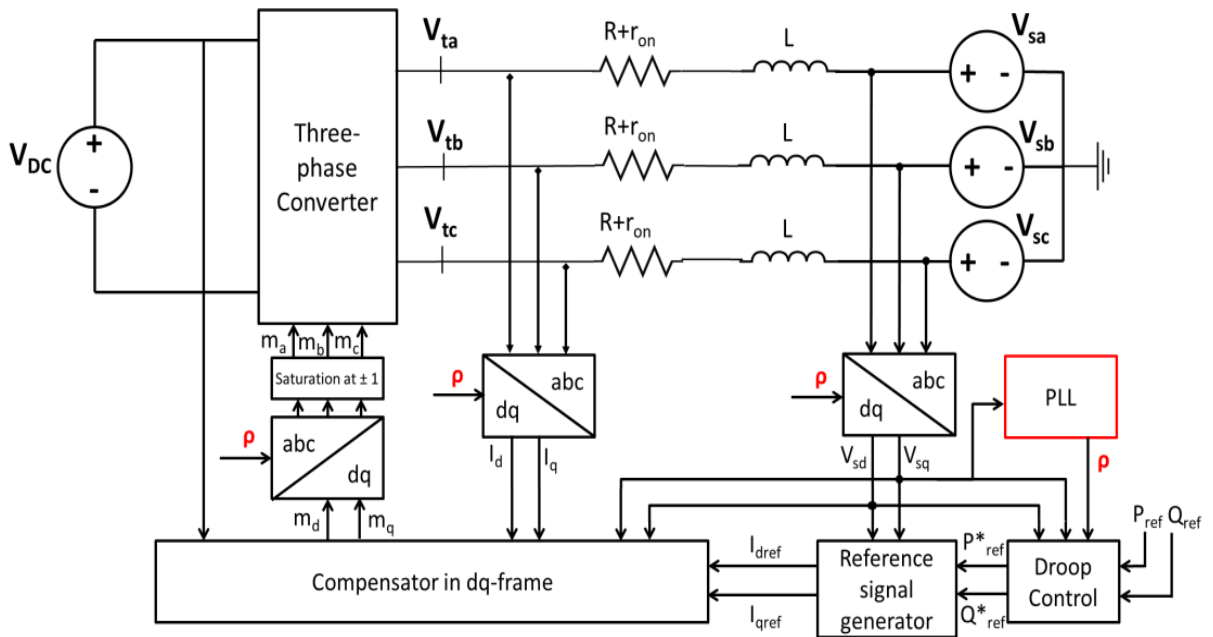
Figure 9 – Schematic Diagram of Current Controlled PQ-PLL Inverter

3.2.1 Current Control in the dq-Frame of the PLL-Based Inverter

The objective of this part is to design a PQ reference PLL based controller. This control Figure 9 is widely studied in literature. A PQ-reference controller has real and reactive power references. That is why a current reference signal generator in the dq-frame is used in where the inputs are $V_{d\_pu}, V_{q\_pu}, P^*_{ref\_pu}, Q^*_{ref\_pu}$.

$$\begin{cases} I_{d\_ref} = \dfrac{2}{3} \dfrac{V_{d\_pu} \times P^*_{ref\_pu} + V_{q\_pu} \times Q^*_{ref\_pu}}{V^2_{d\_pu} + V^2_{q\_pu}} & (3.28) \\[3mm] I_{q\_ref} = \dfrac{2}{3} \dfrac{V_{q\_pu} \times P^*_{ref\_pu} - V_{d\_pu} \times Q^*_{ref\_pu}}{V^2_{d\_pu} + V^2_{q\_pu}} & (3.29) \end{cases}$$

In order to design the current controller, equations derived in the last part are used.

$$\begin{cases} m_d = \dfrac{2}{V_{DC}} (L\dfrac{di_d}{dt} + Ri_d - L\omega I_q + V_{sd}) & (3.30) \\[3mm] m_q = \dfrac{2}{V_{DC}} (L\dfrac{di_q}{dt} + Ri_q + L\omega I_d + V_{sq}) & (3.31) \end{cases}$$

Let's now introduce two control inputs u_d and u_q defined as

$$\begin{cases} u_d = L\dfrac{di_d}{dt} + Ri_d & (3.32) \\[3mm] u_q = L\dfrac{di_q}{dt} + Ri_q & (3.33) \end{cases}$$

Injecting (3.30), (3.31) into (3.32), (3.33) we get:

$$\begin{cases} m_d = \dfrac{2}{V_{DC}} (u_d - L\omega I_q + V_{sd}) & (3.34) \\[3mm] m_q = \dfrac{2}{V_{DC}} (u_q + L\omega I_d + V_{sq}) & (3.35) \end{cases}$$

Now, let's introduce a compensator k_d(s) that processes $e_d = i_{dref} - i_d$ and provides u_d. The same compensator k_q(s) processing $e_q = i_{qref} - i_q$ and providing u_q will be designed. A simple proportional-integral (PI) compensator can easily track ad DC reference command.

$$k_d(s) = k_q(s) = \frac{k_p s + k_i}{s} \tag{3.36}$$

where:

$$\begin{cases} k_p = \dfrac{L}{\tau_i} & \text{(3.37)} \\[2ex] k_i = \dfrac{R}{\tau_i} & \text{(3.38)} \end{cases}$$

where τ_i is the desired time constant.

Finally, a feed-forward filter is added in order to anticipate and compensate pick currents during the connection to the grid which is a low pass filter:

$$G_{ff}(s) = \frac{1}{\tau s + 1} \tag{3.39}$$

where τ is the filter time-constant which needs to be really small (microsecond order) to compensate efficiently. The current control diagram is presented in Figure 10. It is interesting to notice that the output voltage is limited by $\frac{V_{DC}}{2}$.
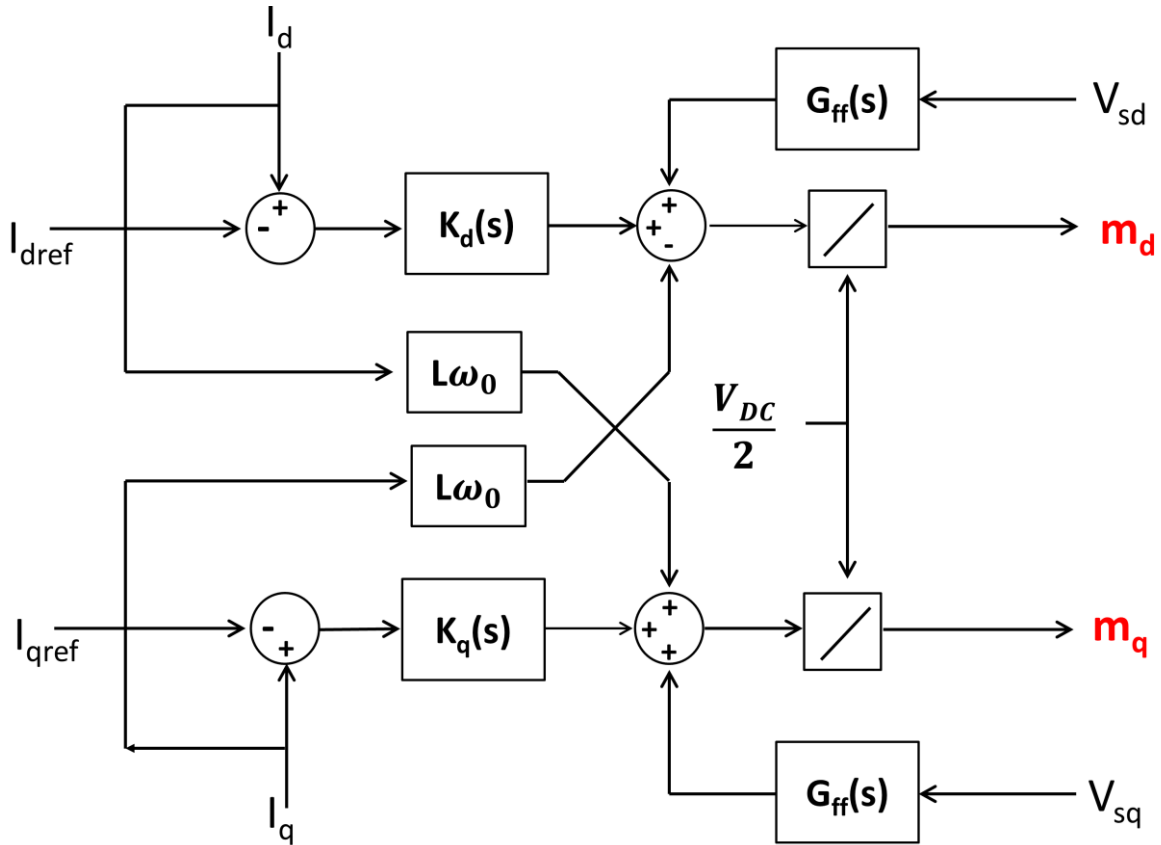
Figure 10 – Current Control Block Diagram

3.2.2 Phase Lock Loop (PLL)

As mentioned, theatrically $\varepsilon(t)$ needs to be equal to $\omega t + \theta_0$ To achieve that performance, the phase-lock-loop (PLL) extracts the frequency from the grid. That frequency will be directly injected into the dq-transform block in order to make the frame rotate at the same speed as the signal.

The frequency measurement is based on the fact that for a balanced system the q-component of the voltage V_{sq} must be equal to 0. That way, $\varepsilon(t)$ has to be set in such way that V_{sq}=0; meaning that the frame is rotating at the same speed as the signal. However, the expression

21

of V_{sq} is a sinusoidal function $V_{sq} = V_s \sin(\omega t + \theta_0 - \varepsilon(t))$, and can't be used directly as a feedback signal to regulate $\varepsilon(t)$. If (t) is initially close enough to $\omega t + \theta_0$ then it is possible to state that V_{sq} $\approx V(\omega t + \theta_0 - \varepsilon(t))$. A possible way to do that is to set $\frac{d\varepsilon}{dt}(0) = \omega_\varepsilon(0) = \omega_0$, ω_0 being the grid's nominal frequency and always keeping ω_ε close enough to ω_0 by putting some boundaries such as

$$\omega_{\varepsilon min} \leq \omega_\varepsilon \leq \omega_{\varepsilon max} \tag{3.40}$$

The phase and frequency are both estimated within a single loop (Figure 11). The studied PLL control loop is composed of a simple PI compensator which has to bring the error $V_{sq0} - V_{sq}$ which is equal to $- V_{sq}$ to 0. The output of the PI compensator is the frequency adjustment. A Voltage-controlled oscillator (VCO) is used as a resettable integrator every time the result of the integration reaches 2π.
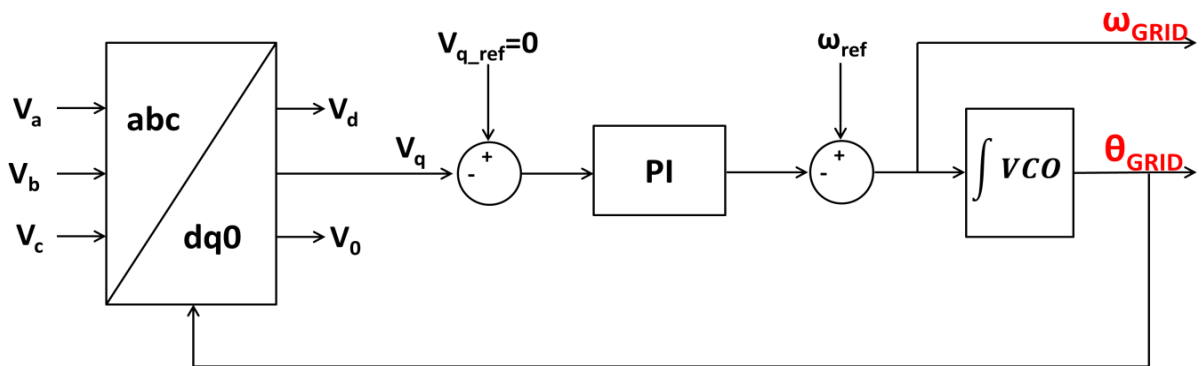
Figure 11 – PLL Structure

3.3 Benchmark #2 – Self-Synchronizing Inverter Control

The self-synchronizing controller has been developed by Joseph Latham, Moath Alqatamin, and Dr. Mcintyre from the University of Louisville with the assistance of Dr. Brandon Grainger and Zachary Smith both from the University of Pittsburgh and is presented in the article "Self-Synchronizing Current Control of a Three-Phase Grid Connected Inverter in the Presence of Unknown Grid Parameters" – IEEE APEC 2020.

3.3.1 General Presentation

A suitable dynamic system model of a three-phase grid connected inverter, as seen in Figure 12, can be modeled in the natural abc-frame as shown in (3.41) where $I_a(t)$, $I_b(t)$, $I_c(t)$ are the three phase currents, V_{dc}, L, and R are the DC-link voltage, filter inductance and resistance, respectively. The control signals are the three-phase duty cycles $D_a(t)$, $D_b(t)$, $D_c(t)$, and the grid parameters are voltage magnitude $V_g(t)$ and grid phase $\theta(t)$. The grid frequency is naturally related to the phase by the following formula: $\omega = \dot{\theta}(t)$. In this paper, the grid phase is unknown so the standard dq-transformation cannot be utilized for (3.41). Instead an estimated γδ-frame is utilized by performing the dq-transformation using $\hat{\theta}(t)$ in place of θ (t), where $\hat{\theta}(t)$ is an observed grid-phase [15] to be designed subsequently. After transformation about $\hat{\theta}(t)$, (3.41) it can be written in the γδ -frame as shown in (**3.42**) where the currents and the control signals have been transformed to the γδ -frame, and the grid-phase estimation error is defined and given in (3.44). Equations (3.45), (3.46) and (3.47), describe the full self-synchronizing controller model. The validity of the current tracking performance is provided in Figure 12. The stability of the controller can be proved by Lyapunov theory.

$$L \begin{bmatrix} \dot{I}_a \\ \dot{I}_b \\ \dot{I}_c \end{bmatrix} = V_{dc} \begin{bmatrix} D_a \\ D_b \\ D_c \end{bmatrix} - R \begin{bmatrix} I_a \\ I_b \\ I_c \end{bmatrix} - V_g \begin{bmatrix} cos(\theta) \\ cos\left(\theta - \dfrac{2\pi}{3}\right) \\ cos\left(\theta + \dfrac{2\pi}{3}\right) \end{bmatrix} \tag{3.41}$$

$$L \begin{bmatrix} \dot{I}_\gamma \\ \dot{I}_\delta \end{bmatrix} = V_{dc} \begin{bmatrix} D_\gamma \\ D_\delta \end{bmatrix} - \begin{bmatrix} R & -\dot{\theta}L \\ \dot{\theta}L & R \end{bmatrix} \begin{bmatrix} I_\gamma \\ I_\delta \end{bmatrix} - V_g \begin{bmatrix} cos\, \tilde{\theta} \\ sin\, \tilde{\theta} \end{bmatrix} \tag{3.42}$$

$$\begin{bmatrix} D_\gamma \\ D_\delta \end{bmatrix} \triangleq \frac{1}{V_{dc}} \left(\begin{bmatrix} R & -\dot{\theta}L \\ \dot{\theta}L & R \end{bmatrix} \begin{bmatrix} I_\gamma \\ I_\delta \end{bmatrix} + \begin{bmatrix} \hat{V}_g \\ 0 \end{bmatrix} + k_1 \begin{bmatrix} \tilde{I}_\gamma \\ \tilde{I}_\delta \end{bmatrix} \right) \tag{3.43}$$

$$\tilde{\theta} \triangleq \theta - \hat{\theta} \tag{3.44}$$

$$\hat{\theta} \triangleq L\tilde{I}_\delta + \int_{t_0}^{t} [\hat{\omega} + (k_1 + 1)\tilde{I}_\delta] \tag{3.45}$$

$$\hat{\omega} \triangleq k_\omega \left(L\tilde{I}_\delta + k_1 \int_{t_0}^{t} \tilde{I}_\delta \right) \tag{3.46}$$

$$\dot{\hat{V}}_g \triangleq k_v \tilde{I}_\gamma \tag{3.47}$$

Figure 12 – General Schematic Diagram of the Current Controlled Self-Synchronizing Inverter

24

3.3.2 Detailed Model

Figure 13 – Three-Phase Inverter Circuit

The first assumption is that we have a three phase balanced system with a single frequency.

$$\begin{bmatrix} e_a \\ e_b \\ e_c \end{bmatrix} = V_g \begin{bmatrix} \cos(\theta) \\ \cos\left(\theta - \dfrac{2\pi}{3}\right) \\ \cos\left(\theta + \dfrac{2\pi}{3}\right) \end{bmatrix} \tag{3.48}$$

where V_g is the amplitude of the grid voltage.

We can generalize the inverter dynamic equation (3.1) to a three phase system:

$$\begin{bmatrix} v_a \\ v_b \\ v_c \end{bmatrix} = L \begin{bmatrix} \dot{I}_a \\ \dot{I}_b \\ \dot{I}_c \end{bmatrix} + R \begin{bmatrix} I_a \\ I_b \\ I_c \end{bmatrix} + \begin{bmatrix} e_a \\ e_b \\ e_c \end{bmatrix} \tag{3.49}$$

Assuming a switching average model where the output voltage is directly proportional to the input

DC voltage through the duty cycle, we have:

$$\begin{bmatrix} v_a \\ v_b \\ v_c \end{bmatrix} = V_{dc} \begin{bmatrix} D_a \\ D_b \\ D_c \end{bmatrix} \tag{3.50}$$

25

where $D_a, D_b, D_c \in [0,1]$. Making these substitutions and rewriting, we can obtain the following three-phase grid current dynamics:

$$L \begin{bmatrix} \dot{I}_a \\ \dot{I}_b \\ \dot{I}_c \end{bmatrix} = V_{dc} \begin{bmatrix} D_a \\ D_b \\ D_c \end{bmatrix} - R \begin{bmatrix} I_a \\ I_b \\ I_c \end{bmatrix} - V_g \begin{bmatrix} \cos(\theta) \\ \cos\left(\theta - \dfrac{2\pi}{3}\right) \\ \cos\left(\theta + \dfrac{2\pi}{3}\right) \end{bmatrix} \tag{3.51}$$

Using the Clarke's transform presented in 3.1.2, we can transfer this model from an abc-frame into a $\alpha\beta$-frame:

$$L \begin{bmatrix} \dot{I}_\alpha \\ \dot{I}_\beta \end{bmatrix} = V_{dc} \begin{bmatrix} D_\alpha \\ D_\beta \end{bmatrix} - R \begin{bmatrix} I_\alpha \\ I_\beta \end{bmatrix} - V_g \begin{bmatrix} \cos\theta \\ \sin\theta \end{bmatrix} \tag{3.52}$$

Similarly, transforming this dynamic model into the dq-frame we obtain:

$$L \begin{bmatrix} \dot{I}_d \\ \dot{I}_q \end{bmatrix} = V_{dc} \begin{bmatrix} D_d \\ D_q \end{bmatrix} - \begin{bmatrix} R & -\omega L \\ \omega L & R \end{bmatrix} \begin{bmatrix} I_d \\ I_q \end{bmatrix} - V_g \begin{bmatrix} 1 \\ 0 \end{bmatrix} \tag{3.53}$$

where $\omega \triangleq \dot{\theta}$.

3.3.3 Estimated Reference Frame Model

Since the angle θ is unknown, the dq transformation will be executed using an observer $\hat{\theta}$ that will be presented subsequently. This new transformation is denoted as $\gamma\delta$. For this purpose the following modified dq transformation is defined:

$$\begin{bmatrix} f_\gamma \\ f_\delta \end{bmatrix} = \hat{K}_P \begin{bmatrix} f_\alpha \\ f_\beta \end{bmatrix} \tag{3.54}$$

where:

$$\widehat{K}_P \triangleq \begin{bmatrix} \cos\widehat{\theta} & \sin\widehat{\theta} \\ -\sin\widehat{\theta} & \cos\widehat{\theta} \end{bmatrix} \qquad (3.55)$$

and for future reference the following inverse transformation:

$$\begin{bmatrix} f_\alpha \\ f_\beta \end{bmatrix} = \widehat{K}_P^{-1} \begin{bmatrix} f_\gamma \\ f_\delta \end{bmatrix} \qquad (3.56)$$

where:

$$\widehat{K}_P^{-1} = \begin{bmatrix} \cos\widehat{\theta} & -\sin\widehat{\theta} \\ \sin\widehat{\theta} & \cos\widehat{\theta} \end{bmatrix} \qquad (3.57)$$

An error for the angle observer can be defined as:

$$\tilde{\theta} \triangleq \theta - \widehat{\theta} \qquad (3.58)$$

Using the inverse of this transformation we can substitute the $\alpha\beta$ vectors in the $\alpha\beta$-frame model

for $\gamma\delta$ vectors such as:

$$L\frac{d}{dt}\left(\widehat{K}_P^{-1} \begin{bmatrix} I_\gamma \\ I_\delta \end{bmatrix}\right) = V_{dc}\widehat{K}_P^{-1} \begin{bmatrix} D_\gamma \\ D_\delta \end{bmatrix} - R\widehat{K}_P^{-1} \begin{bmatrix} I_\gamma \\ I_\delta \end{bmatrix} - V_g \begin{bmatrix} \cos\theta \\ \sin\theta \end{bmatrix} \qquad (3.59)$$

Multiplying both sides by $\widehat{K}_P$, we obtain:

$$L\widehat{K}_P\frac{d}{dt}\left(\widehat{K}_P^{-1} \begin{bmatrix} I_\gamma \\ I_\delta \end{bmatrix}\right) = V_{dc}\widehat{K}_P\widehat{K}_P^{-1} \begin{bmatrix} D_\gamma \\ D_\delta \end{bmatrix} - R\widehat{K}_P\widehat{K}_P^{-1} \begin{bmatrix} I_\gamma \\ I_\delta \end{bmatrix} - V_g\widehat{K}_P \begin{bmatrix} \cos\theta \\ \sin\theta \end{bmatrix} \qquad (3.60)$$

following simplifications will help to clarify the model:

27

$$\widehat{K}_P \widehat{K}_P^{-1} = I_2 \tag{3.61}$$

$$\widehat{K}_P \begin{bmatrix} \cos\theta \\ \sin\theta \end{bmatrix} = \begin{bmatrix} \cos\tilde{\theta} \\ \sin\tilde{\theta} \end{bmatrix} \tag{3.62}$$

$$\frac{d}{dt}\left(\widehat{K}_P^{-1}\begin{bmatrix} I_\gamma \\ I_\delta \end{bmatrix}\right) = \widehat{K}_P^{-1}\begin{bmatrix} \dot{I}_\gamma \\ \dot{I}_\delta \end{bmatrix} + \dot{\widehat{K}}_P^{-1}\begin{bmatrix} I_\gamma \\ I_\delta \end{bmatrix} \tag{3.63}$$

where:

$$\dot{\widehat{K}}_P^{-1} = \dot{\hat{\theta}}\begin{bmatrix} -\sin\hat{\theta} & -\cos\hat{\theta} \\ \cos\hat{\theta} & -\sin\hat{\theta} \end{bmatrix} \tag{3.64}$$

Making these substitutions into the model we obtain:

$$L\begin{bmatrix} \dot{I}_\gamma \\ \dot{I}_\delta \end{bmatrix} + L\widehat{K}_P\dot{\widehat{K}}_P^{-1}\begin{bmatrix} I_\gamma \\ I_\delta \end{bmatrix} = V_{dc}\begin{bmatrix} D_\gamma \\ D_\delta \end{bmatrix} - R\begin{bmatrix} I_\gamma \\ I_\delta \end{bmatrix} - V_g\begin{bmatrix} \cos\tilde{\theta} \\ \sin\tilde{\theta} \end{bmatrix} \tag{3.65}$$

We can further calculate

$$\widehat{K}_P\dot{\widehat{K}}_P^{-1} = \dot{\hat{\theta}}\begin{bmatrix} 0 & -1 \\ 1 & 0 \end{bmatrix} \tag{3.66}$$

Substituting this into the above and combining terms we obtain the following $\gamma\delta$-frame current dynamics:

$$L\begin{bmatrix} \dot{I}_\gamma \\ \dot{I}_\delta \end{bmatrix} = V_{dc}\begin{bmatrix} D_\gamma \\ D_\delta \end{bmatrix} - \begin{bmatrix} R & -\dot{\hat{\theta}}L \\ \dot{\hat{\theta}}L & R \end{bmatrix}\begin{bmatrix} I_\gamma \\ I_\delta \end{bmatrix} - V_g\begin{bmatrix} \cos\tilde{\theta} \\ \sin\tilde{\theta} \end{bmatrix} \tag{3.67}$$

3.3.4 Controller Development

3.3.4.1 Assumptions

1. Alpha-beta frame currents I_α, I_β are known

2. Parameters R, L, V_{dc} are known *a priori* and are constants with respect to time.

3. The grid frequency ω and amplitude V_g are unknown but are assumed to be positive constants. Grid phase θ is also unknown.

3.3.4.2 Observer Objectives and Description

- Sensorlessly identify the phase angle θ of the grid, i.e. ensure that $\hat{\theta} \to \theta, \tilde{\theta} \to 0$.

  Controller Objectives

- Achieve the reference current values I_γ^*, I_δ^*. When $\tilde{\theta} = 0$, $I_\gamma = I_d$ and $I_\delta = I_q$, meaning reactive and real power can be achieved through equations (3.28) and (3.29) control error is defined as:

$$\begin{bmatrix} \tilde{I}_\gamma \\ \tilde{I}_\delta \end{bmatrix} \triangleq \begin{bmatrix} I_\gamma^* \\ I_\delta^* \end{bmatrix} - \begin{bmatrix} I_\gamma \\ I_\delta \end{bmatrix} \tag{3.68}$$

Taking the derivative of these error equations and substituting in the $\gamma\delta$ current dynamics we obtain the following open loop error dynamics (assuming a fix current reference):

$$L \begin{bmatrix} \dot{\tilde{I}}_\gamma \\ \dot{\tilde{I}}_\delta \end{bmatrix} = \begin{bmatrix} R & -\dot{\hat{\theta}}L \\ \dot{\hat{\theta}}L & R \end{bmatrix} \begin{bmatrix} I_\gamma \\ I_\delta \end{bmatrix} + V_g \begin{bmatrix} \cos\tilde{\theta} \\ \sin\tilde{\theta} \end{bmatrix} - V_{dc} \begin{bmatrix} D_\gamma \\ D_\delta \end{bmatrix} \tag{3.69}$$

To facilitate the analysis, we make that the error $\tilde{\theta}$ is small and centered about 0. Therefore:

$$L\begin{bmatrix} \dot{I}_\gamma \\ \dot{I}_\delta \end{bmatrix} = \begin{bmatrix} R & -\dot{\hat{\theta}}L \\ \dot{\hat{\theta}}L & R \end{bmatrix}\begin{bmatrix} I_\gamma \\ I_\delta \end{bmatrix} + V_g\begin{bmatrix} 1 \\ \sin\tilde{\theta} \end{bmatrix} - V_{dc}\begin{bmatrix} D_\gamma \\ D_\delta \end{bmatrix} \tag{3.70}$$

Based on this equation and the estimation of the grid voltage magnitude $\hat{V}_g$, we can define the following duty cycle control inputs:

$$\begin{bmatrix} D_\gamma \\ D_\delta \end{bmatrix} \triangleq \frac{1}{V_{dc}}\left(\begin{bmatrix} R & -\dot{\hat{\theta}}L \\ \dot{\hat{\theta}}L & R \end{bmatrix}\begin{bmatrix} I_\gamma \\ I_\delta \end{bmatrix} + \begin{bmatrix} \hat{V}_g \\ 0 \end{bmatrix} + k_1\begin{bmatrix} \tilde{I}_\gamma \\ \tilde{I}_\delta \end{bmatrix}\right) \tag{3.71}$$

where $\hat{V}_g$ is an estimate of the grid voltage amplitude.

The angle observer and frequency estimate will be designed in the stability analysis (Appendix B).

4.0 Droop Control Purpose and Implementation

In order to have a consistent comparison, a PQ reference (Figure 14) has been set on the self-synchronizing inverter control. In order to calculate I_{d_ref} (3.28) and I_{q_ref} (3.29), the PLL controlled inverter will operate with the measured grid voltage while the self-synchronizing inverter control scheme will make use of the estimated-voltage; thus, the self- synchronizing inverter requires less sensing hardware (i.e. no voltage sensors). Furthermore, droop control has been added to ensure time-variant references for the real and reactive power so the inverter is responsible for adjusting its generation in accordance with the main grid consumption. The frequency is linked to the real power through the droop coefficient R_p Figure 14 and the voltage is correlated to the reactive power through R_q.
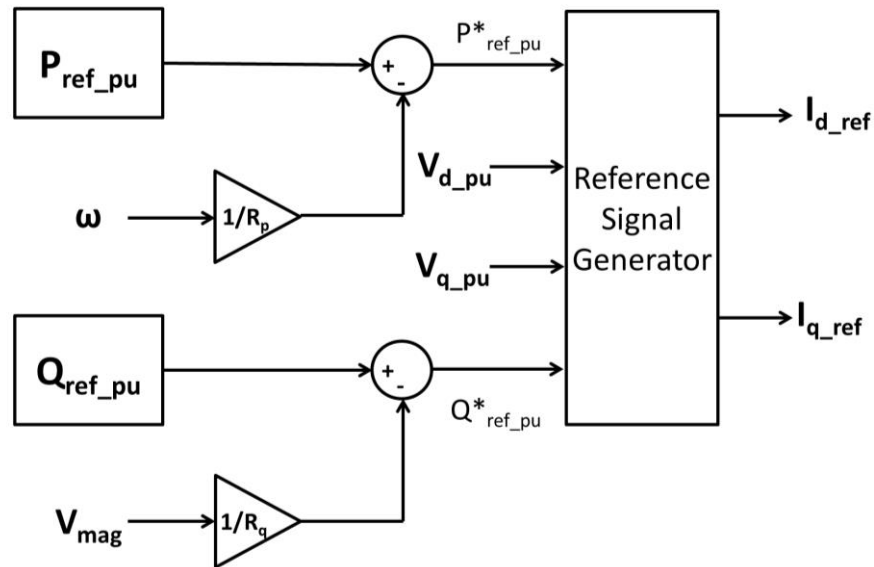

Figure 14 – Droop Control Implementation

5.0 Simulations Results and Analysis

5.1 Inverter Validation Simulations

5.1.1 PQ Inverter Control with a PLL (PQ-PLL)

The following circuit, Figure 15, has been used in PLECS in order to validate the PQ-PLL inverter's control. A particular emphasis will be given to the current control. At time t_0 the reference power will experience a 10% drop.
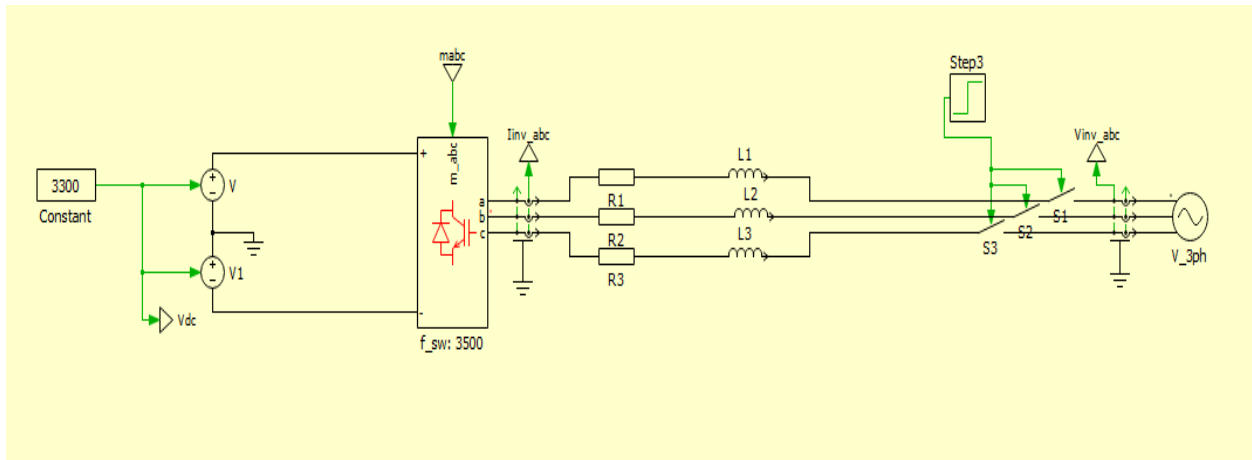

Figure 15 – PQ Inverter with a PLL PLECS Model

Table 1 – PQ Inverter with a PLL Simulation Parameters

R_{filter}	$1.63 \times 10^{-3}\,\Omega$	$k_{p_{PLL}}$	2
L_{filter}	$100 \times 10^{-6}\,H$	$k_{i_{PLL}}$	10
V_{grig_pp}	3.3 kV	$k_{p_{kd}}$	0.05
f_{grid}	60 Hz	$k_{i_{kd}}$	0.815
V_{DC}	5 kV	$k_{p_{kq}}$	0.05
$f_{switching}$	$25 \times 10^{3}\,Hz$	$k_{i_{kq}}$	0.815
$\tau_{G_{ff}}$	$8.10^{-7}\,s$		

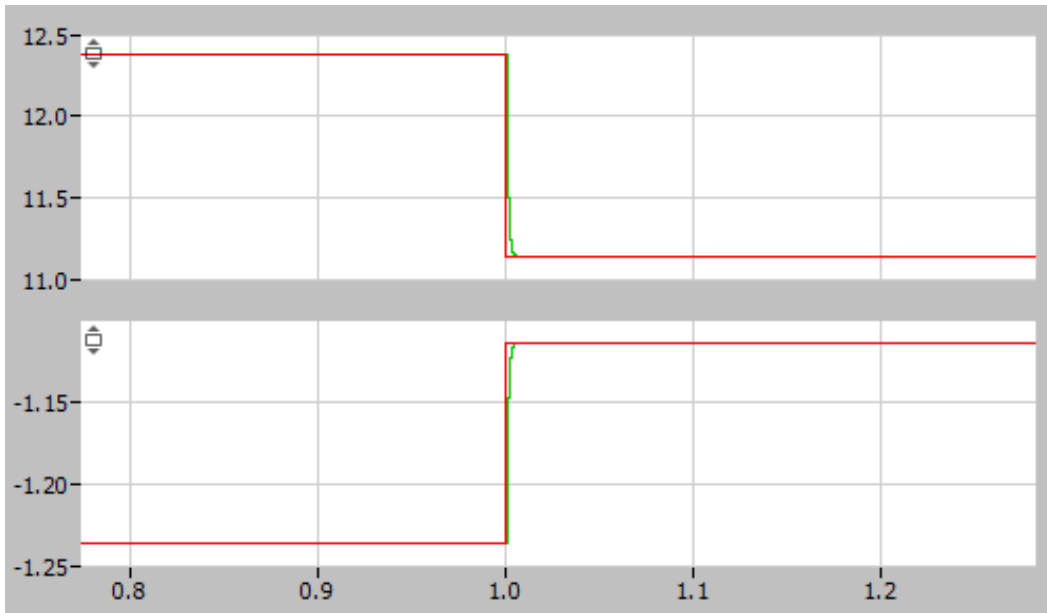**Figure 16 – PQ Inverter with a PLL Current Controller**

Figure 17 – PQ Inverter with a PLL Current Tracking Performances with the d (up) and q (down) Current

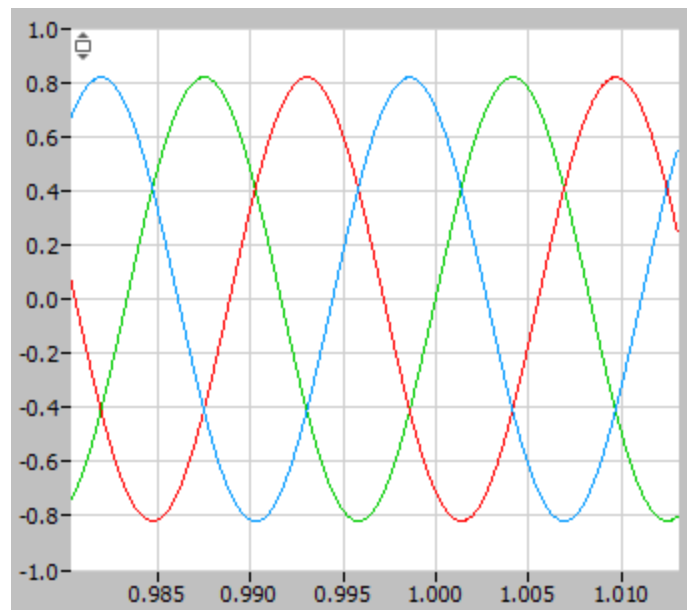**Reference in Red and the Mesured Current in Green**

Figure 18 – PQ Inverter with a PLL - abc Modulation Indexes

We can see on Figure 17 that the current follows the reference current and the modulation index (Figure 18) is sinusoidal and its magnitude is inferior to 1.

In conclusion, the simulations validate the presented PQ-PLL inverter control.

5.1.2 PQ Self-Synchronizing Inverter Control

The following circuit, Figure 19, has been used in PLECS in order to validate the self-synchronizing inverter's control. A particular emphasis will be given to the current control. At time t_0 the reference power will experience a 10% drop.
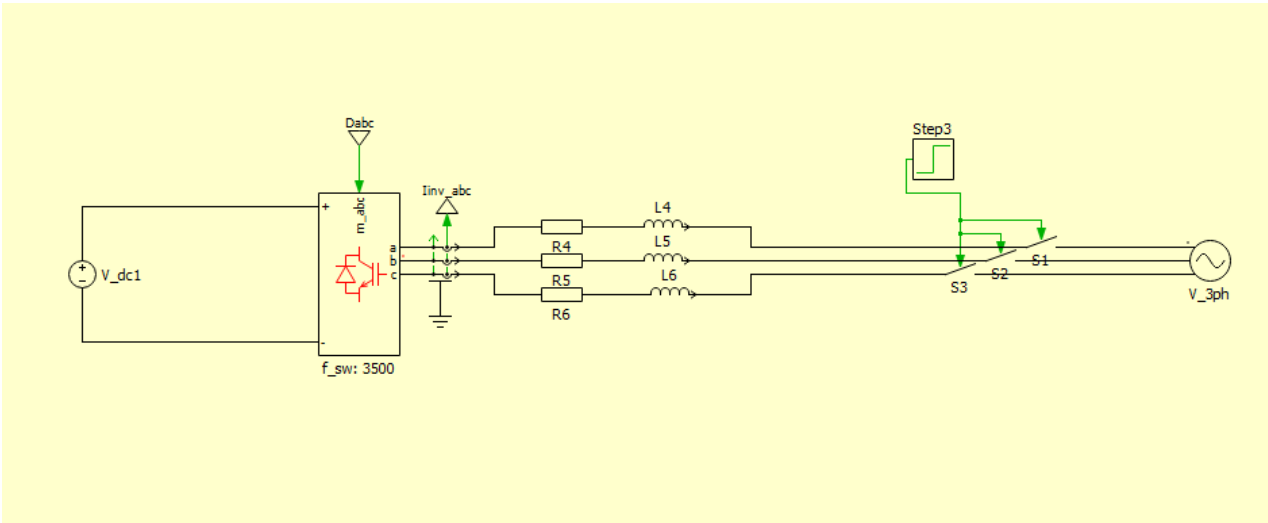

Figure 19 – PQ Self-Synchronizing Inverter PLECS Model

Table 2 – PQ Self-Synchronizing Inverter Simulation Parameters

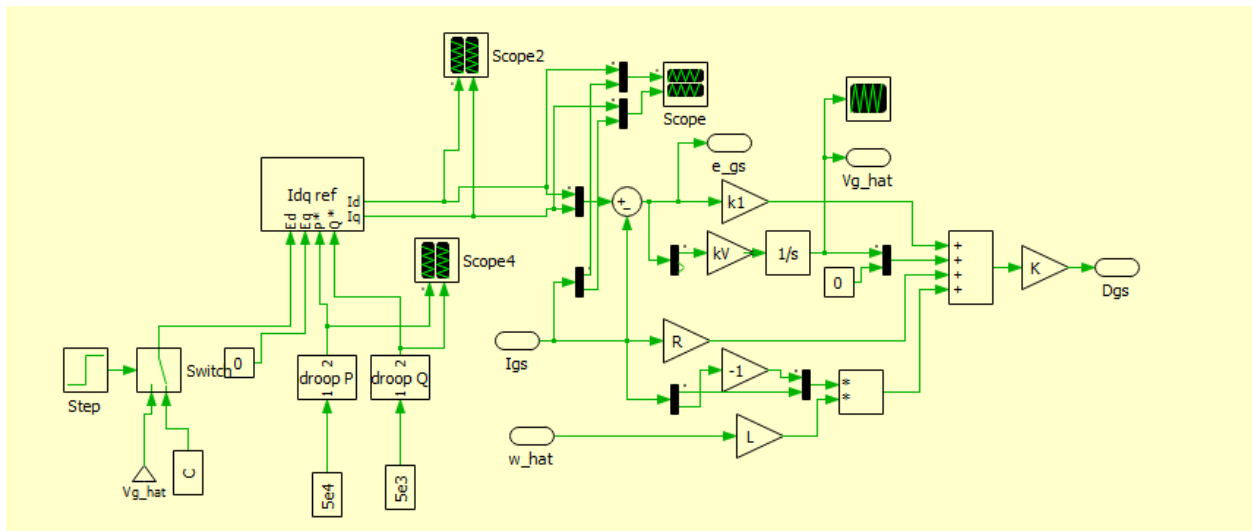| R_{filter}	0.1 Ω	$K1$	2x10^{-5}
L_{filter}	0.01 H	K	20
V_{grig_pp}	3.3 kV	KV	1000
f_{grid}	60 Hz	Kw	100
$f_{switching}$	25x10^3 Hz	V_{DC}	5 kV

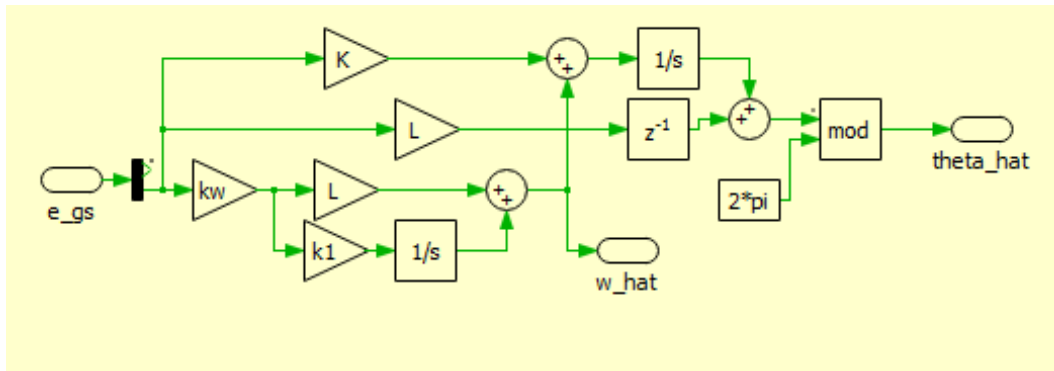**Figure 20 – PQ Self-Synchronizing Inverter Current Controller**

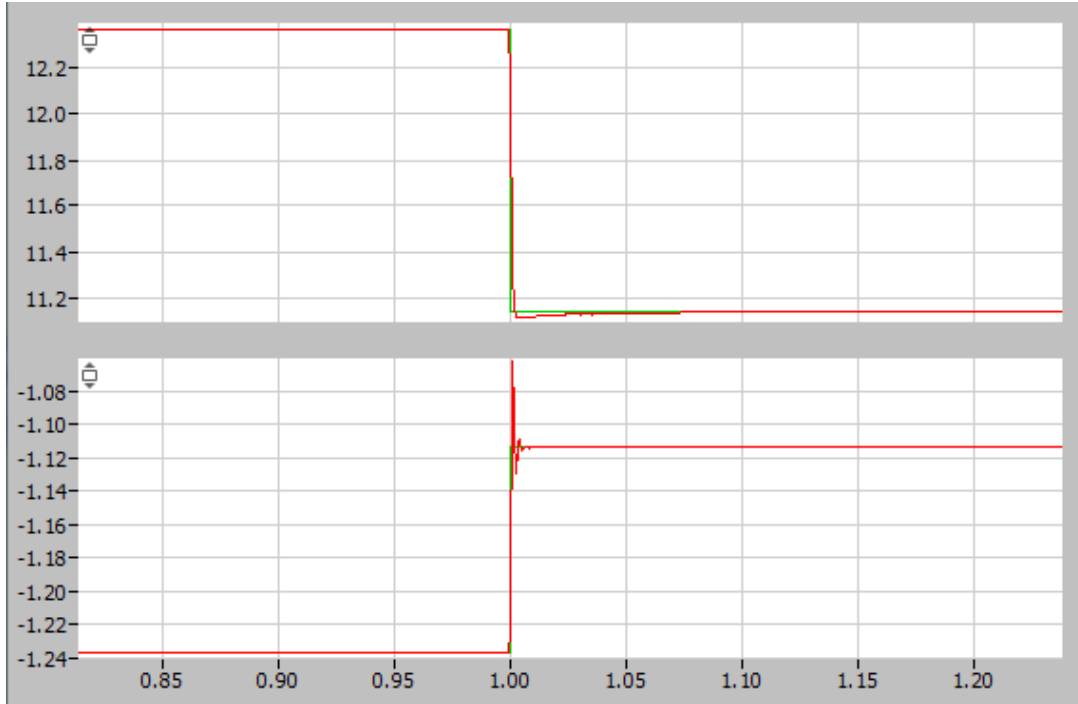**Figure 21 – PQ Self-Synchronizing Inverter Angle Observer**

Figure 22 – PQ Self-Synchronizing Inverter Current Tracking Performances with the d (up) and q (down)

Current Reference in Red and the Mesured Current in Green
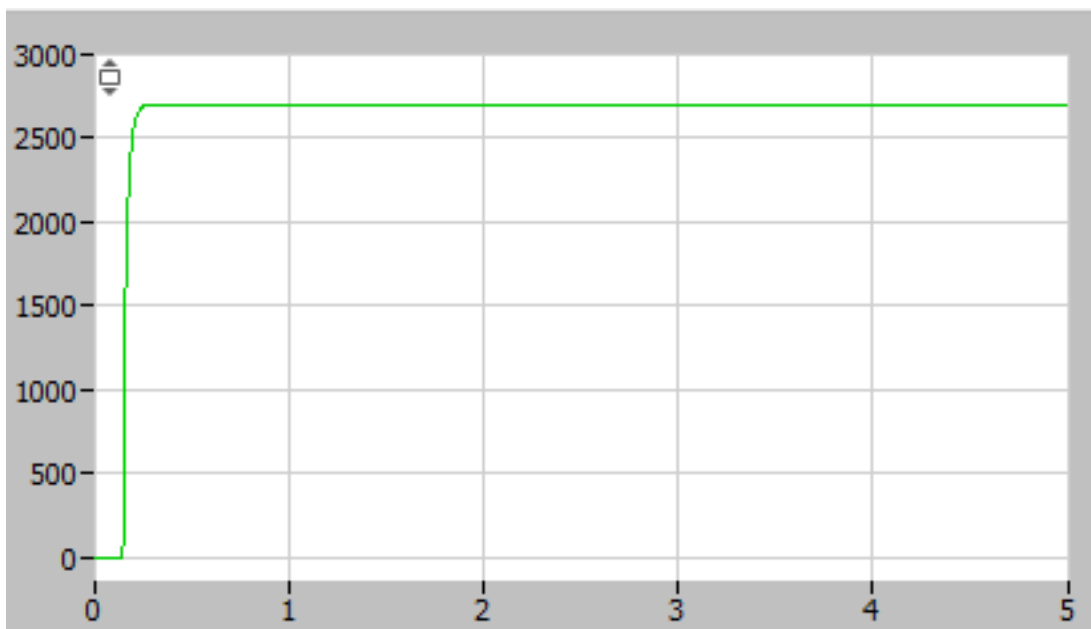

Figure 23 – PQ Self-Synchronizing Inverter Voltage Estimation

We can see that the current follows the reference current (Figure 22) and that the estimate voltage is equal, after initialization, to the grid voltage (Figure 23).

In conclusion, the simulations validate the presented self-synchronizing inverter control.

5.2 System Frequency Dynamic Response in a High Renewable Penetration Grid Simulation Parameters

In order to study the system frequency dynamic response for each inverter case (PQ-PLL and self-synchronizing inverter) a high renewable penetration grid has been built on PLECS (Figure 24) based on chapter 2.0. The penetration ratio (Pr) and the inertia (H) are two parameters that are tuned in order to study the frequency behavior for those cases.

Simulations, which consist in dropping the load by 10% at time t_0 in order to study the grid's frequency dynamic behavior, has been carried out in PLECS (time step of 50µs) and normalized by (5.1) for interpretation. Equation (5.1) is the frequency normalization that was applied in this work, where f_o is 60Hz and $f_{steady-state}$ is frequency after load change.

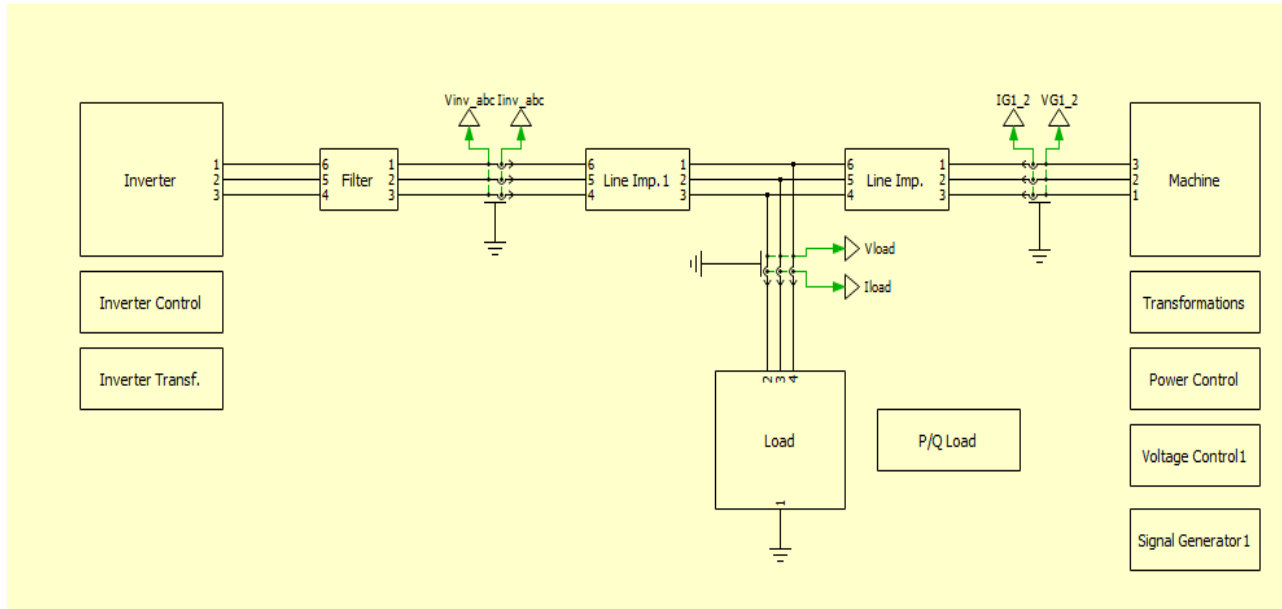$$f(i)_{norm} = \frac{f(i) - f_0}{f_{steady-state} - f_0} \qquad (5.1)$$

Figure 24 – Grid Model PLECS

For both inverter's simulations the grid, and particularly the synchronous generator, parameters, excluding the inverter itself, are the same. The following table shows all the main parameters.

Table 3 – Full Grid Model Parameters

General Grid parameters			
$V_{grig-pp}$	3.3 kV	R_{Line}	≈ 0
f_{grid}	60 Hz	L_{Line}	≈ 0
R_{droop_P}	5%	*Load change*	10%
R_{droop_Q}	5%		
Machine parameters			
T_g	0.1s	H	$2-6$ s
K_{CH}, K_G	1	D	0.01
T_{ch}	1s	K_a	1
V_{ref_pu}	1	τ_{kl}	0.02 s
ω_{ref}	$2\pi60$ rad.s^{-1}	K_E	0.05
K_f	0	T_E	0.46
PQ-PLL Inverter parameters			
R_{filter}	1.63x10^{-3} Ω	$\tau_{G_{ff}}$	8.10^{-7} s
L_{filter}	100x10^{-6} H	$k_{p_{kd}}$	0.05
$f_{switching}$	25x10^3 Hz	$k_{i_{kd}}$	0.815
$k_{p_{PLL}}$	2	$k_{p_{kq}}$	0.05
$k_{i_{PLL}}$	10	$k_{i_{kq}}$	0.815
V_{DC}	5 kV		
Self-synchronizing Inverter parameters			
R_{filter}	0.1 Ω	KV	1000
L_{filter}	0.01 H	Kw	100
$f_{switching}$	25x10^3 Hz	$K1$	20
K	2x10^{-5}	V_{DC}	10 kV

5.3 Results and Analysis

Results are presented for the 4 extreme cases:

- Case (a): Pr=20%, H=2
- Case (a): Pr=20%, H=2
- Case (a): Pr=20%, H=2
- Case (a): Pr=20%, H=2

Additional results are presented in the Appendix A. All results have been taken in consideration for the analysis.

Table 4 - PLL (Classic) and Self-Synchronizing (Adaptive) Frequency Response for Pr=20% and 80% and H=2 and 6.

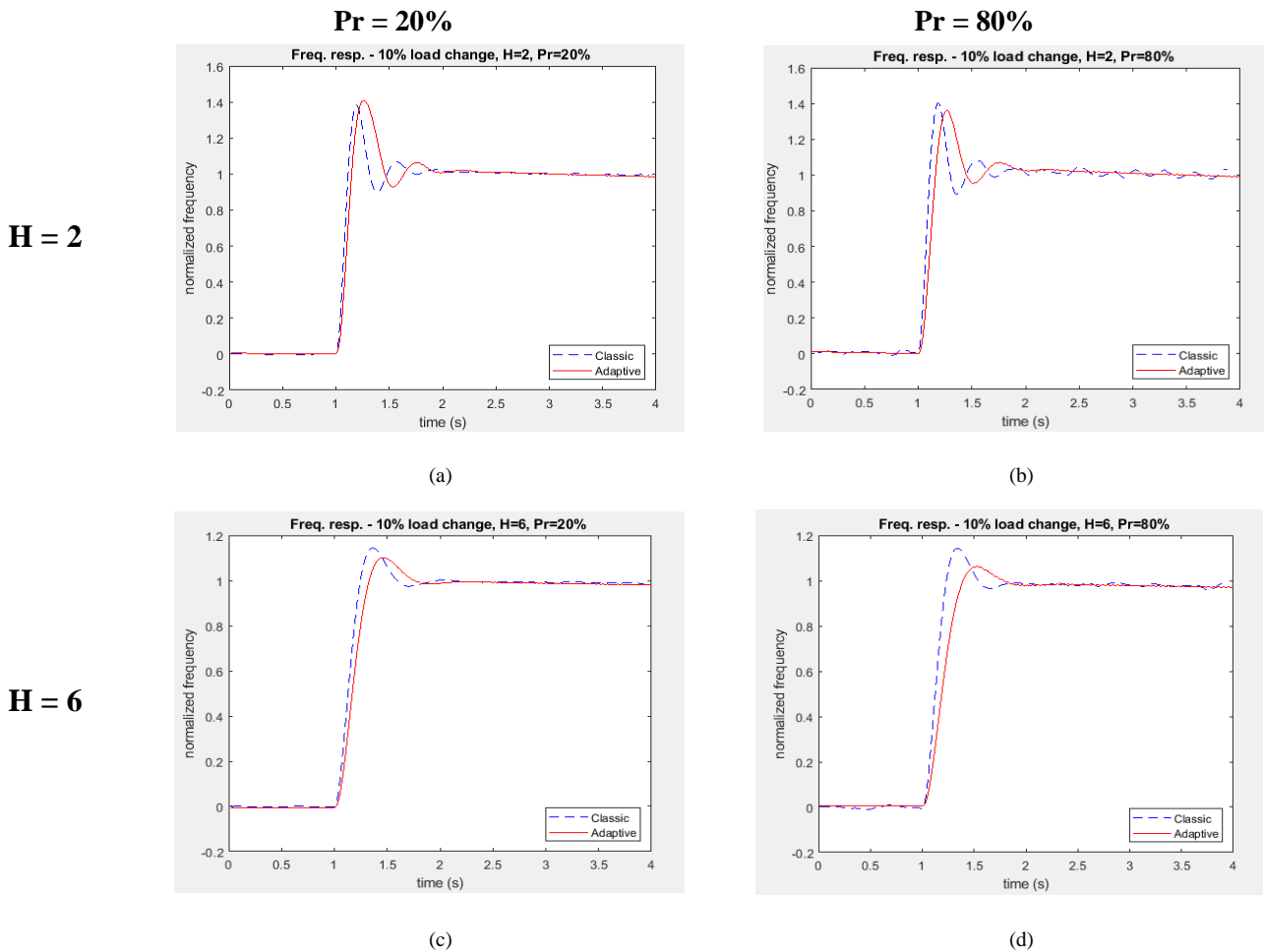Pr = 20%   Pr = 80%

H = 2

(a)   (b)

H = 6

(c)   (d)

Table 5 - Overshoot, Undershoot and Steady-State Ripple for PLL (Classic - Blue) and Self-Synchronizing (Adaptive - Red) Controls for Pr=20% and 80% and H=2 and 6 Extremities

	Max overshoot (%)		Max undershoot (%)		Steady-state ripple p-p (%)	
	PLL	*Self-Synch*	*PLL*	*Self-Synch*	*PLL*	*Self-Synch*
Case (a): *Pr=20%, H=2*	38.0	41.1	10.1	7.3	1.2	<0.1
Case (b): *Pr=80%, H=2*	40.1	36.2	10.6	4.5	4.2	<0.1
Case (c): *Pr=20%, H=6*	14.3	10.1	2.5	1.5	<0.1	<0.1
Case (d): *Pr=80%, H=6*	14.5	6.3	4.5	2.1	1.5	<0.1

5.3.1 Impact of Mechanical Inertia

Mechanical inertia has a similar impact on both the PQ-PLL and self-synchronizing controlled inverter grid's frequency overshoot. Increasing the inertia lowers the overshoot. For example, as seen in Table 4 and Table 5, for the *Pr*=20% case, a 41.1% overshoot for the self-synchronized inverter with *H*=2 (Table 4 - a) is observed and only 10.1% with *H*=6 (Table 4 - c). Another interesting observation is the hunting effect that is observed for the lower inertia, high penetration PLL case (Table 4 - b) compared to the self-synchronizing routine. In addition, despite a higher overshoot in Fig. 5a, the self-synchronized inverter has a second undershoot swing 30% lower (7.3% against 10.1%) compared to the PQ-PLL inverter. In line with these results, it can be concluded that both inverters' overshoot is directly linked to inertia. However, the self-synchronizing controlled inverter has significantly faster dynamics and a steady-state that is always reached in less than a second while the PLL controlled inverters cannot reach steady-state within 3 seconds for low inertia, high penetration grids (Table 4 - b).

5.3.2 Impact of Renewable Source Penetration Ratio

The renewable source penetration ratio has a direct impact on the grid's frequency behavior for each of the inverter scenarios evaluated. Increasing the penetration ratio for the PLL based control inverter increases the overshoot. For example, for *H*=2, a +2.1% overall overshoot is observed when increasing *Pr* from 20% (Table 4 - a) to 80% (Table 4 - b). This result was already observed in [5]. On the other hand, for the self-synchronizing inverter, increasing *Pr* tends to reduce the overshoot. For example, for *H*=6 (Table 4 - b), a -8.2% overall overshoot is observed by increasing *Pr* from 20% (Table 4 - c) to 80% (Table 4 - d); the overshoot of Table 4 – d is reduced by half compared to Table 4 - c. This key result can be explained by the self-synchronizing control itself. Elevating the penetration ratio, *Pr*, strengthens the role of the inverter control; hence, the inverter's adaptive control depends only the current error signals and works to minimize these current errors. In contrast, the classic PQ-PLL controlled inverter depends on the transient response of its PLL reaching a new steady-state value in the face of frequency disturbances. Then the current control scheme within the classic scheme adjusts achieve its control objective. The new approach removes the slow-response time of the classic cascaded control scheme and achieves current control in the presence of uncertain grid parameters.

6.0 Conclusion

A self-synchronizing inverter control has been introduced in this article. After describing the grid-model, the grid dynamic frequency response to a 10% load change was examined for a system including PQ-PLL inverters and a new self-synchronizing inverter. First, increasing the mechanical inertia lowers the frequency overshoot. The self-synchronizing inverter reaches steady-state significantly faster due to the internal dynamics of the adaptive control by disrupting the need for a cascaded control scheme. Secondly, increasing the renewable source penetration ratio tends to increase the overshoot for PLL based inverters while considerably lowering the overshoot for the self- synchronizing inverters because the adaptive control only depends on the current control errors signals and not a separate system response. Based upon this study, the self-synchronizing inverter can improve the performance of traditional inverter topologies in high renewable penetration (low inertia) environments.

7.0 Future Work

Future studies can be done on a larger scale grid with a significant number of synchronous machines and inverter-based sources for a more detailed transient analysis and an improved frequency dynamic studies.

Another important factor to be studied is the interaction between the PLL based inverter and the self-synchronizing one. In this study we only modeled inverter 100% PQ-PLL controlled or self-synchronized. It would be interesting to integrate both inverters into the model at the same time and mathematically describe their interaction. This analysis is crucial since PQ-PLL inverters are already installed and those controls won't be changed. That's why introducing the self-synchronizing inverter would be progressive and the "cohabitation" with the PQ-PLL inverters will be necessary. Predicting this interaction can definitely avoid issues caused by both inverter types interactions.

Finally, unbalanced conditions need to be taken in account in future works. Faults are an important component of power system studies. In that case V_q component will be different of 0 so some adjustments need to be done both in the PLL and self-synchronizing controls. Then a stability study needs to be done to confirm the self-synchronizing inverter design in fault conditions.

Appendix A Detailed Results

Additional results are presented in this section. The model and the parameters are the same that in section 5.2 System Frequency Dynamic Response in a High Renewable Penetration Grid Simulation Parameters.

The penetration ration (Pr) is equal to 20%, 50%, 80%. For each case, Inertia (H) is equal to 2,4,6. These results have been taken in account for previous analysis.
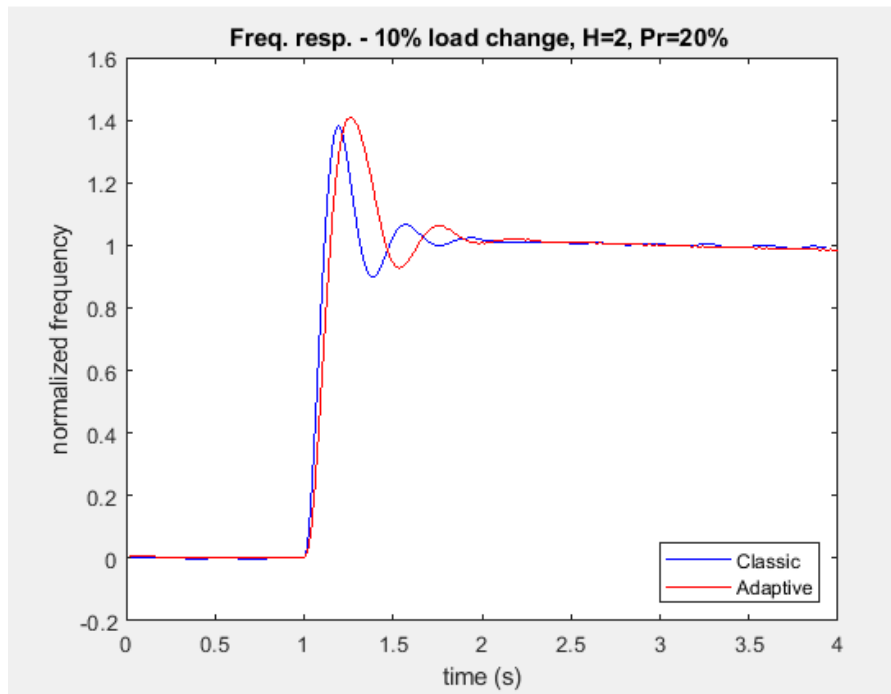
Appendix A.1 Results for Pr=20%
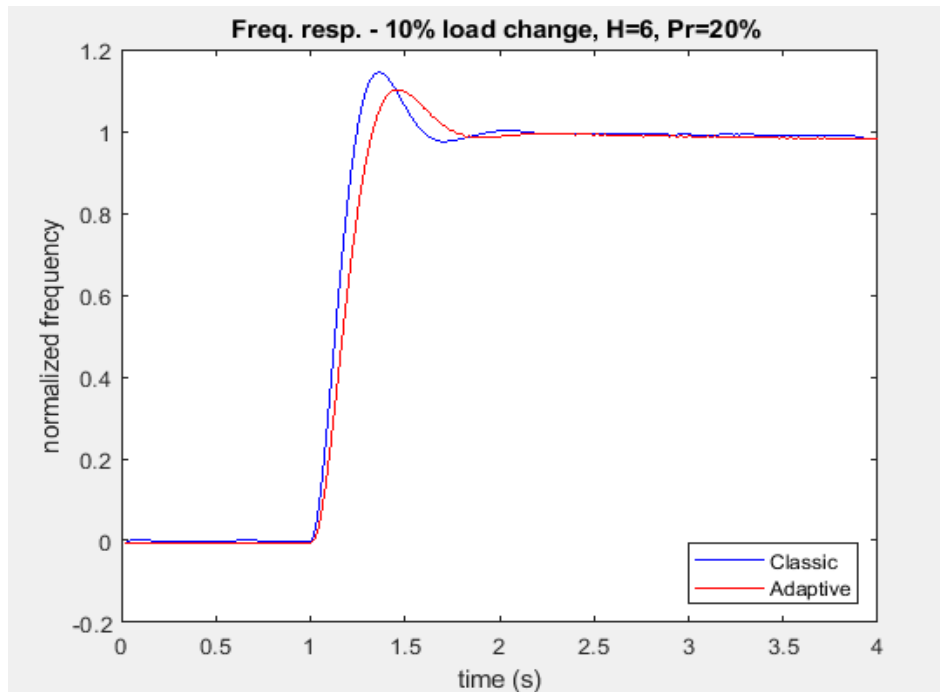
Appendix Figure 1 - Normalized Frequency Response to a 10% Load Change Pr=20% & H=6
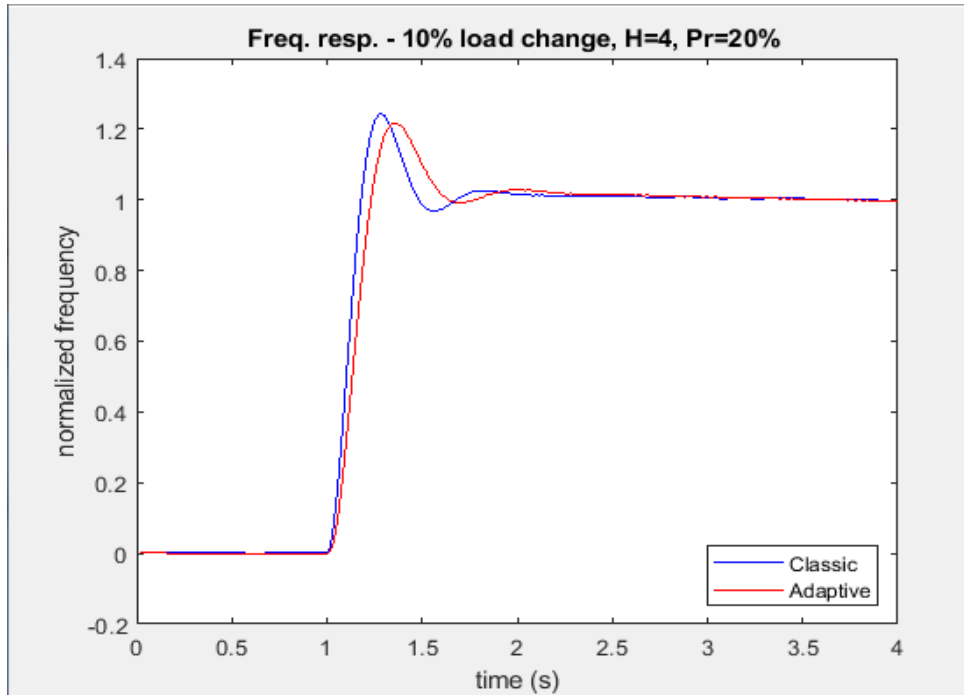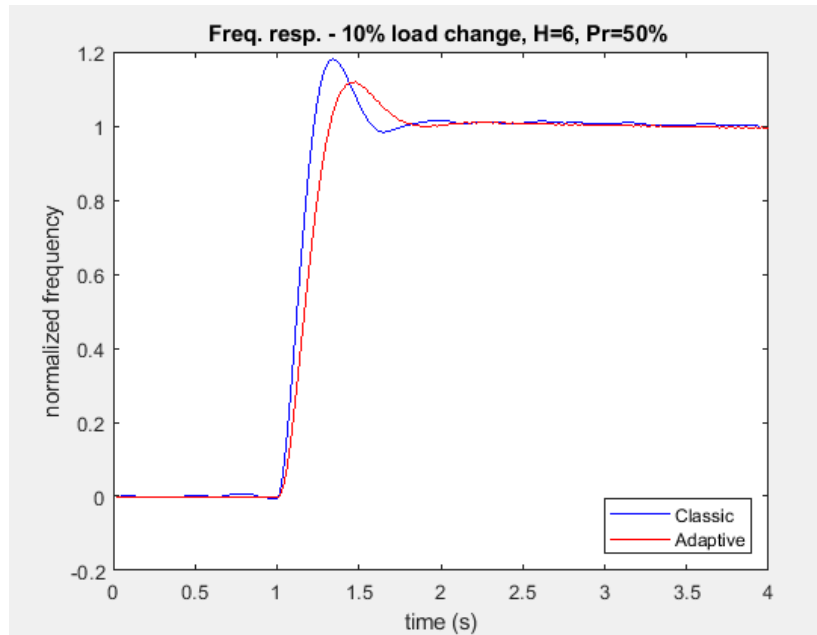
Appendix Figure 2 - Normalized Frequency Response to a 10% Load Change Pr=20% & H=4

Appendix Figure 3 - Normalized Frequency Response to a 10% Load Change Pr=20% & H=2

Appendix A.2 Results for Pr=50%

Appendix Figure 4 - Normalized Frequency Response to a 10% Load Change Pr=50% & H=4

Appendix Figure 5 - Normalized Frequency Response to a 10% Load Change Pr=50% & H=4

Appendix Figure 6 - Normalized Frequency Response to a 10% Load Change Pr=50% & H=2

Appendix A.3 Results for Pr=80%

Appendix Figure 7 - Normalized Frequency Response to a 10% Load Change Pr=80% & H=6

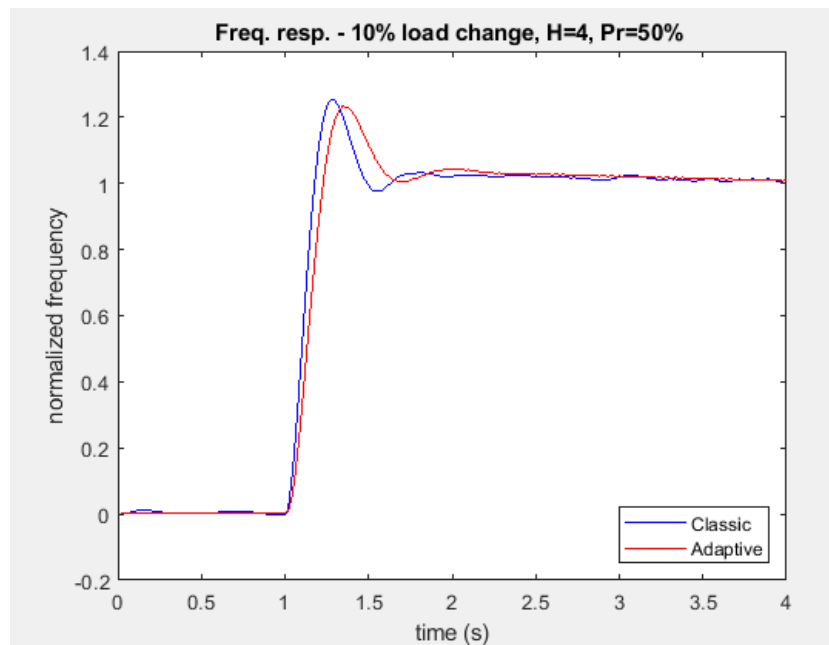**Appendix Figure 8 - Normalized Frequency Response to a 10% Load Change Pr=80% & H=4**

Appendix Figure 9 - Normalized Frequency Response to a 10% Load Change Pr=80% & H=2
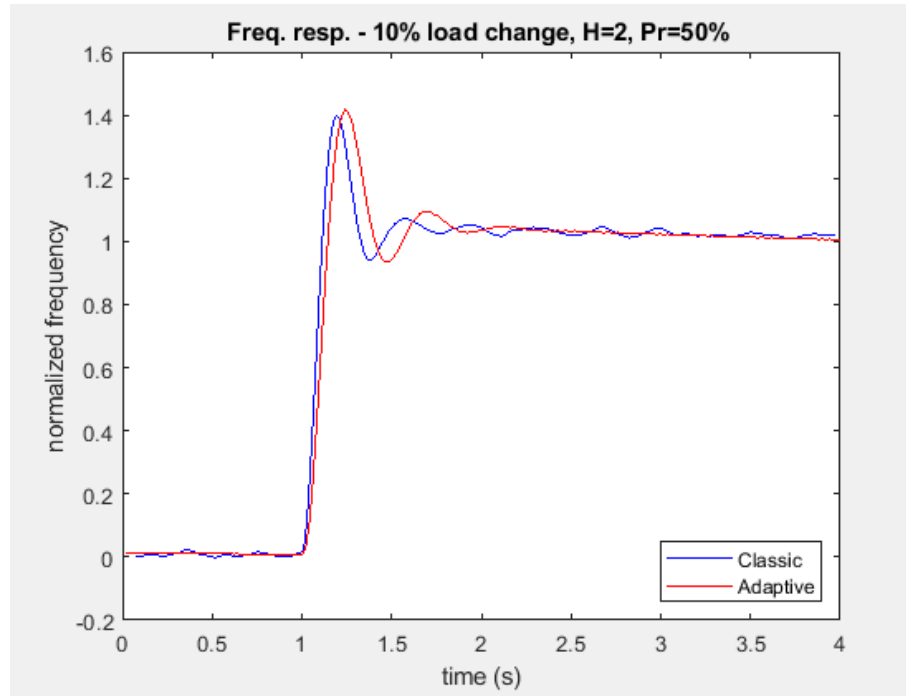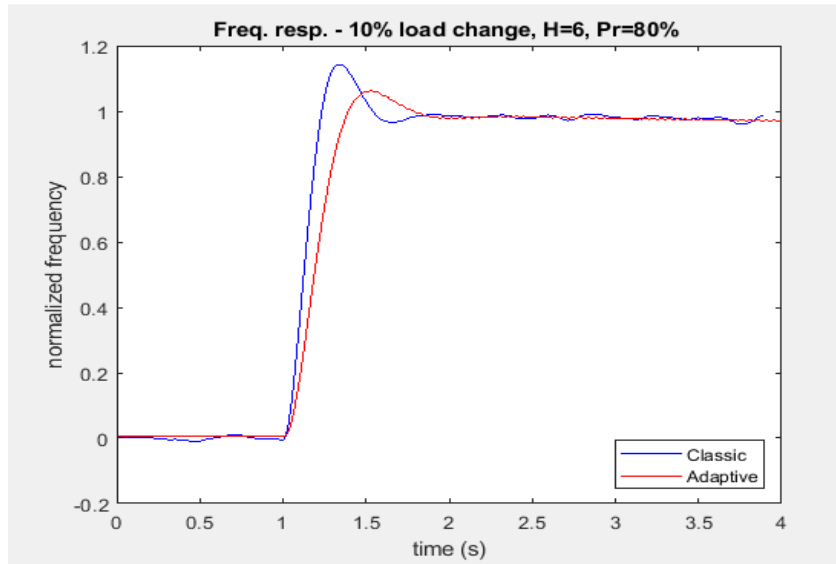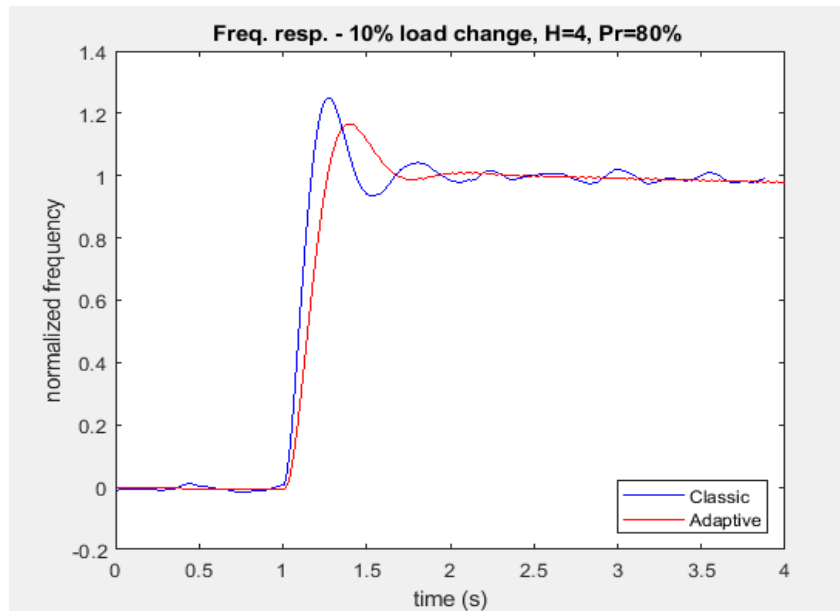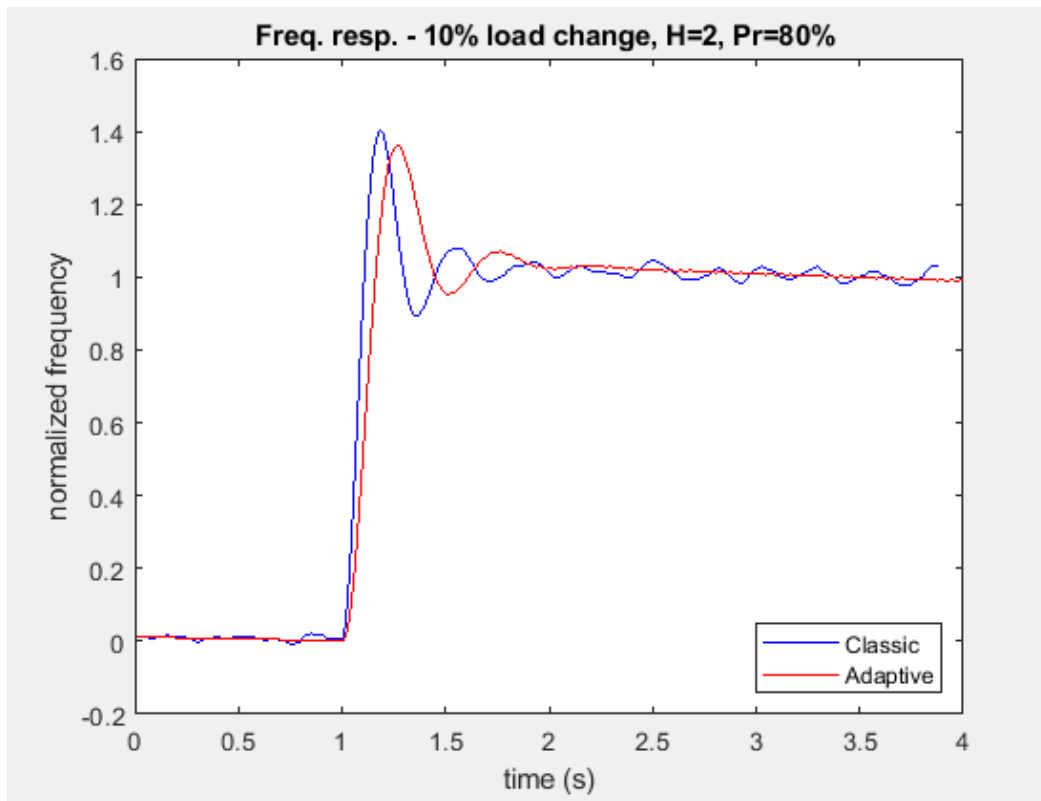
Appendix B Stability Analysis of the Self-Synchronizing Controller

Based on the article [16] we can study the self-synchronizing controller stability.

Substituting (3.71) into (3.67) we obtain the following closed loop current error dynamics

$$L \begin{bmatrix} \dot{\tilde{I}}_\gamma \\ \dot{\tilde{I}}_\delta \end{bmatrix} = -k_1 \begin{bmatrix} \tilde{I}_\gamma \\ \tilde{I}_\delta \end{bmatrix} + \begin{bmatrix} \tilde{V}_g \\ V_g \sin \tilde{\theta} \end{bmatrix} \tag{1}$$

where $\tilde{V}_g$ is the estimate error defined as $\tilde{V}_g \triangleq V_g - \hat{V}_g$, which has the following error dynamic based on Assumption 3 in 3.3.4.1:

$$\dot{\tilde{V}}_g = -\dot{\hat{V}}_g. \tag{2}$$

We can rewrite the δ-axis equation above to obtain the following useful relationship:

$$V_g \sin \tilde{\theta} = k_1 \tilde{I}_\delta + L \dot{\tilde{I}}_\delta \tag{3}$$

Taking the derivative of $\tilde{\theta}$ we have:

$$\dot{\tilde{\theta}} = \omega - \dot{\hat{\theta}} \tag{4}$$

We also define a speed estimate $\hat{\omega}$, with corresponding error $\tilde{\omega} \triangleq \omega - \hat{\omega}$, which has the following error dynamic based on Assumption 3 in 3.3.4.1:

$$\dot{\tilde{\omega}} = -\dot{\hat{\omega}} \tag{5}$$

To design the angle and frequency observer let's define a Lyapunov function:

$$V = \frac{1}{2}L\tilde{I}_\gamma{}^2 + \frac{1}{2}L\tilde{I}_\delta{}^2 + V_g(1 - \cos\tilde{\theta}) + \frac{1}{2k_\omega}\tilde{\omega}^2 + \frac{1}{2k_V}\tilde{V}_g^2 \qquad (6)$$

We can see from Assumption 3 (3.3.4.1) that this equation is positive definite in the local region $\tilde{\theta} \in (-2\pi, 2\pi)$. Assuming that $\tilde{\theta}$ is wrapped such that its effective domain is $\tilde{\theta} \in [-\pi, \pi)$ we can see that the function is effectively globally positive definite. Taking the derivative of this function we find:

$$\dot{V} = L\tilde{I}_\gamma\dot{\tilde{I}}_\gamma + L\tilde{I}_\delta\dot{\tilde{I}}_\delta + V_g\dot{\tilde{\theta}}\sin\tilde{\theta} + \frac{1}{k_\omega}\tilde{\omega}\dot{\tilde{\omega}} + \frac{1}{k_V}\tilde{V}_g\dot{\tilde{V}}_g \qquad (7)$$

Then substituting into this the dynamics for each error signal:

$$V\dot{V} = \tilde{I}_\gamma\left(-k_1\tilde{I}_\gamma + \tilde{V}_g\right) + \tilde{I}_\delta\left(-k_1\tilde{I}_\delta + V_g\sin\tilde{\theta}\right) + V_g\sin\tilde{\theta}\left(\omega - \dot{\hat{\theta}}\right) - \frac{1}{k_\omega}\tilde{\omega}\dot{\hat{\omega}} - \frac{1}{k_V}\tilde{V}_g\dot{\hat{V}}_g \quad (8)$$

This form motivates the following design for the angle observer update law:

$$\dot{\hat{\theta}} \triangleq \hat{\omega} + \tilde{I}_\delta + V_g\sin\tilde{\theta}_e \qquad (9)$$

We can see that this design is unrealizable due to the unknown signals comprising the 3rd term on the RHS. To make this observer realizable we can make a substitution for the last term based on the CLED for $\tilde{I}_\delta$ to obtain:

$$\dot{\hat{\theta}} \triangleq \hat{\omega} + (k_1 + 1)\tilde{I}_\delta + L\dot{\tilde{I}}_\delta \qquad (10)$$

and then integrate both sides yielding the following realizable form:

$$\hat{\theta} = L\tilde{I}_\delta + \int [\hat{\omega} + (k_1 + 1)\tilde{I}_\delta] \tag{11}$$

where $\hat{\omega}$ is still to be designed. Note that we do not have a realizable form of $\dot{\hat{\theta}}$, which is necessary for our D_γ, D_δ duty cycle control inputs. For this reason, we are compelled to use the subsequently designed $\hat{\omega}$ in its place. Given the relationship between these variables, this substitution is easily justified.

Substituting the unrealizable form of $\dot{\hat{\theta}}$ into the earlier $\dot{V}$ equation and simplifying we obtain:

$$\dot{V} = -k_1\tilde{I}_\gamma^2 + \tilde{I}_\gamma\tilde{V}_g - k_1\tilde{I}_\delta^2 - V_g^2 \sin^2 \tilde{\theta} + \tilde{\omega}V_g \sin \tilde{\theta} - \frac{1}{k_\omega}\tilde{\omega}\dot{\hat{\omega}} - \frac{1}{k_V}\tilde{V}_g\dot{\hat{V}}_g \tag{12}$$

This then motivates the following unrealizable design for the speed estimator:

$$\dot{\hat{\omega}} = k_\omega V_g \sin \tilde{\theta} \tag{13}$$

To obtain a realizable form of this estimator we can use the same substitution as before along with integration of both sides to obtain:

$$\hat{\omega} = k_\omega \left(L\tilde{I}_\delta + k_1 \int \tilde{I}_\delta \right) \tag{14}$$

Substituting the unrealizable form into the $\dot{V}$ equation and simplifying we have:

$$\dot{V} = -k_1\tilde{I}_\gamma^2 + \tilde{I}_\gamma\tilde{V}_g - k_1\tilde{I}_\delta^2 - V_g^2 \sin^2 \tilde{\theta} - \frac{1}{k_V}\tilde{V}_g\dot{\hat{V}}_g \tag{15}$$

54

Finally, we can design the adaptive voltage amplitude as:

$$\dot{\hat{V}}_g \triangleq k_V \tilde{I}_\gamma \qquad (16)$$

which results in the following $\dot{V}$:

$$\dot{V} = -k_1 \tilde{I}_\gamma^2 - k_1 \tilde{I}_\delta^2 - V_g^2 \sin^2 \tilde{\theta} \qquad (17)$$

We can see that $\dot{V}(t)$ is a negative semi-definite function.

From the form of $V(t), \dot{V}(t)$ we can conclude that $\tilde{I}_\gamma, \tilde{I}_\delta, \sin^2 \tilde{\theta}, \tilde{\omega}_e \in \mathcal{L}_\infty$.

- Since $\tilde{I}'_d, \tilde{\theta}_e \in \mathcal{L}_\infty$ we can see from CLED for $\tilde{I}'_d$ that $\dot{\tilde{I}}'_d \in \mathcal{L}_\infty$.

- Since $\tilde{\omega}_e \in \mathcal{L}_\infty$ and from Assumption 3 $\omega_e \in \mathcal{L}_\infty$ we can see that $\hat{\omega}_e \in \mathcal{L}_\infty$

- Since $\tilde{I}'_d, \tilde{\theta}_e, \hat{\omega}_e \in \mathcal{L}_\infty$ we can see from definition of $\dot{\hat{\theta}}_e$ that $\dot{\hat{\theta}}_e \in \mathcal{L}_\infty$

- Since $\omega_e, \dot{\hat{\theta}}_e \in \mathcal{L}_\infty$ we can see from definition of $\dot{\tilde{\theta}}_e$ that $\dot{\tilde{\theta}}_e \in \mathcal{L}_\infty$

- Since $\dot{\tilde{I}}'_d, \dot{\tilde{\theta}}_e \in \mathcal{L}_\infty$ we can see that $\ddot{V} \in \mathcal{L}_\infty$, thus we can use Barbalat's Lemma to show that $\dot{V}(t) \to 0$ as $t \to \infty$ and thus that $\tilde{I}'_d, \tilde{\theta}_e \to 0$ as $t \to \infty$ as well.

Bibliography

[1] P. R. D. Federal Ministry for Economic Affairs and Energy, "The Energy of the Future – Sixth 'Energy Transition' Monitoring Report , Reporting Year 2016 – Summary," 2018.

[2] A. Kwasinski, W. Weaver, and R. S. Balog, *Microgrids and other Local Area Power and Energy Systems*. Cambridge: Cambridge University Press, 2016.

[3] J. M. Guerrero, M. Chandorkar, T. Lee, and P. C. Loh, "Advanced Control Architectures for Intelligent Microgrids—Part I: Decentralized and Hierarchical Control," *IEEE Trans. Ind. Electron.*, vol. 60, no. 4, pp. 1254–1262, 2013.

[4] B. Kroposki *et al.*, "Achieving a 100% Renewable Grid: Operating Electric Power Systems with Extremely High Levels of Variable Renewable Energy," *IEEE Power Energy Mag.*, vol. 15, no. 2, pp. 61–73, 2017.

[5] D. Pattabiraman, R. H. Lasseter., and T. M. Jahns, "Comparison of Grid Following and Grid Forming Control for a High Inverter Penetration Power System," in *2018 IEEE Power & Energy Society General Meeting (PESGM)*, 2018, pp. 1–5.

[6] R. Rosso, G. Buticchi, M. Liserre, Z. Zou, and S. Engelken, "Stability analysis of synchronization of parallel power converters," in *IECON 2017 - 43rd Annual Conference of the IEEE Industrial Electronics Society*, 2017, pp. 440–445.

[7] D. Dong, B. Wen, D. Boroyevich, P. Mattavelli, and Y. Xue, "Analysis of Phase-Locked Loop Low-Frequency Stability in Three-Phase Grid-Connected Power Converters Considering Impedance Interactions," *IEEE Trans. Ind. Electron.*, vol. 62, no. 1, pp. 310–321, Jan. 2015.

[8] Y. Sun *et al.*, "The Impact of PLL Dynamics on the Low Inertia Power Grid: A Case Study of Bonaire Island Power System," *Energies*, vol. 12, no. 7, p. 1259, Apr. 2019.

[9] R. Rosso, M. Andresen, S. Engelken, and M. Liserre, "Analysis of the Interaction Among Power Converters Through Their Synchronization Mechanism," *IEEE Trans. Power Electron.*, pp. 1–1, 2019.

[10] Qing-Chang Zhong, Phi-Long Nguyen, Zhenyu Ma, and Wanxing Sheng, "Self-Synchronized Synchronverters: Inverters Without a Dedicated Synchronization Unit," *IEEE Trans. Power Electron.*, vol. 29, no. 2, pp. 617–630, Feb. 2014.

[11] D. Pattabiraman, R. H. Lasseter., and T. M. Jahns, "Comparison of Grid Following and Grid Forming Control for a High Inverter Penetration Power System," in *2018 IEEE Power & Energy Society General Meeting (PESGM)*, 2018, pp. 1–5.

[12]   A. Bergen and V. Vitall, *Power Systems Analysis*, 2nd Editio. Pearson, 2000.

[13]   "IEEE Recommended Practice for Excitation System Models for Power System Stability Studies," *IEEE Std 421.5-2005 (Revision of IEEE Std 421.5-1992)*. pp. 1–93, 2006.

[14]   A. Yazdani and R. Iravani, "8.4 Current-Mode Control of Real-/Reactive-Power Controller," in *Voltage-Sourced Converters in Power Systems : Modeling, Control, and Applications*, 1 edition., Wiley-IEEE Press, 2010.

[15]   G. C. Konstantopoulos, Q. Zhong, and W. Ming, "PLL-Less Nonlinear Current-Limiting Controller for Single-Phase Grid-Tied Inverters: Design, Stability Analysis, and Operation Under Grid Faults," *IEEE Trans. Ind. Electron.*, vol. 63, no. 9, pp. 5582–5591, 2016.

[16]   J. Latham, M. Alqatamin, Z. T. Smith, B. M. Grainger, and and M. McIntyre, "Self-Synchronizing Current Control of a Three-Phase GridConnected Inverter in the Presence of Unknown Grid Parameters," *IEEE Appl. Power Electron. Conf. Expo.*, 2020.